iScience

CellPress
OPEN ACCESS

Article

Highly Controllable and Silicon-Compatible Ferroelectric Photovoltaic Synapses for Neuromorphic Computing

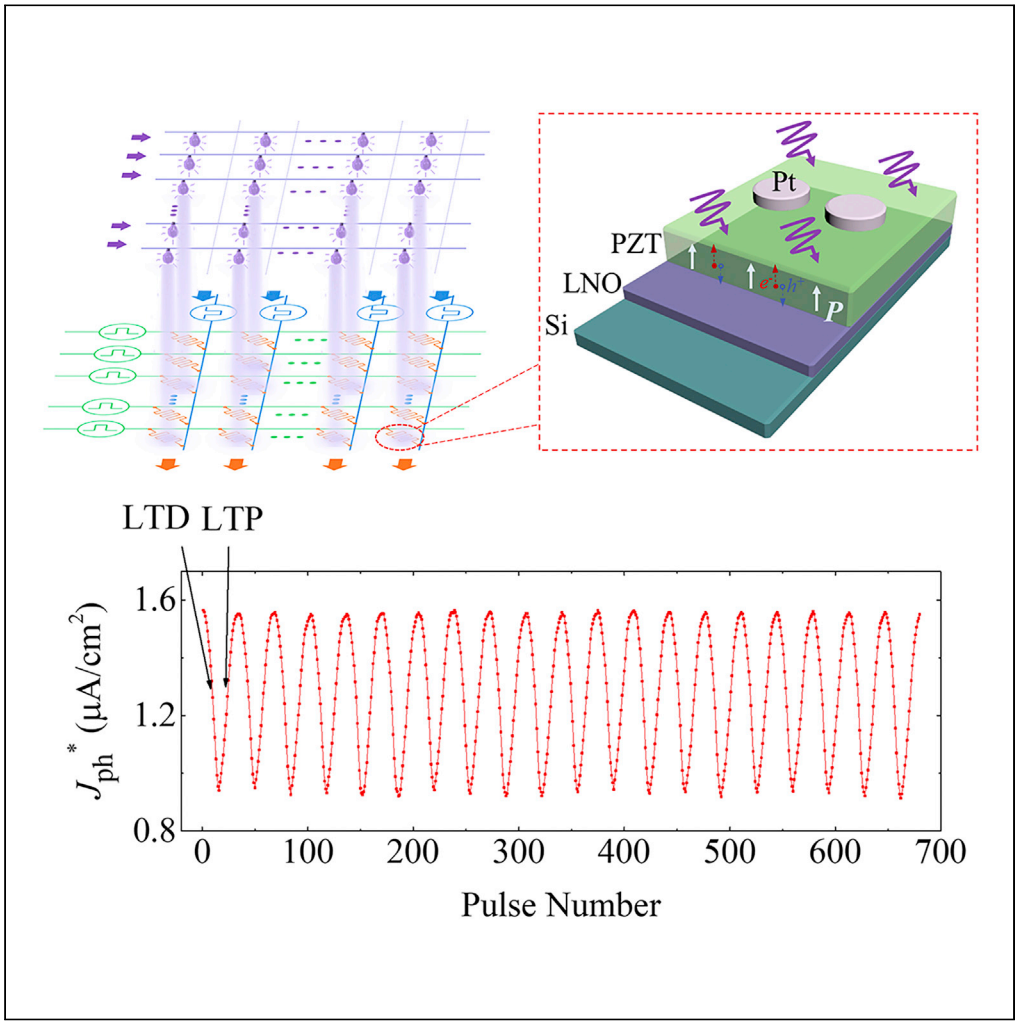

Shengliang Cheng, Zhen Fan, Jingjing Rao, ..., Guoliang Yuan, Xingsen Gao, Jun-Ming Liu

fanzhen@m.scnu.edu.cn

HIGHLIGHTS

Switchable ferroelectric photovoltaic (FePV) effect is used for synaptic application

Tunable photovoltaic response is enabled by gradual polarization switching

Versatile synaptic functions and high image recognition accuracy are achieved

The FePV synapses are facilely grown on silicon substrates

Cheng et al., iScience *23*, 101874
December 18, 2020
https://doi.org/10.1016/j.isci.2020.101874

iScience

CellPress
OPEN ACCESS

Article

Highly Controllable and Silicon-Compatible Ferroelectric Photovoltaic Synapses for Neuromorphic Computing

Shengliang Cheng,[1,2] Zhen Fan,[1,2,7,*] Jingjing Rao,[1] Lanqing Hong,[3] Qicheng Huang,[1] Ruiqiang Tao,[1] Zhipeng Hou,[1] Minghui Qin,[1] Min Zeng,[1] Xubing Lu,[1] Guofu Zhou,[2,4] Guoliang Yuan,[5] Xingsen Gao,[1] and Jun-Ming Liu[1,6]

SUMMARY

Ferroelectric synapses using polarization switching (a purely electronic switching process) to induce analog conductance change have attracted considerable interest. Here, we propose ferroelectric photovoltaic (FePV) synapses that use polarization-controlled photocurrent as the readout and thus have no limitations on the forms and thicknesses of the constituent ferroelectric and electrode materials. This not only makes FePV synapses easy to fabricate but also reduces the depolarization effect and hence enhances the polarization controllability. As a proof-of-concept implementation, a Pt/Pb($Zr_{0.2}Ti_{0.8}$)O_3/$LaNiO_3$ FePV synapse is facilely grown on a silicon substrate, which demonstrates continuous photovoltaic response modulation with good controllability (small nonlinearity and write noise) enabled by gradual polarization switching. Using photovoltaic response as synaptic weight, this device exhibits versatile synaptic functions including long-term potentiation/depression and spike-timing-dependent plasticity. A simulated FePV synapse-based neural network achieves high accuracies (>93%) for image recognition. This study paves a new way toward highly controllable and silicon-compatible synapses for neuromorphic computing.

INTRODUCTION

The human brain can outperform the most advanced digital computer in many intellectual tasks, such as image and voice recognition, data classification, and associative learning (Drachman, 2005; Banerjee et al., 2017; Kuzum et al., 2013; Markram, 2012). Moreover, the human brain consumes only ~20 W power to perform an intellectual task, which is at least three orders of magnitude lower than that of the digital computer (Eryilmaz et al., 2015; Yang et al., 2018b). Therefore, the brain-inspired neuromorphic computing is considered as a very promising computing architecture in the coming era of artificial intelligence. The learning in the brain is enabled by the ability of synapses (Figure 1A) to strengthen or weaken their connection strengths (or weights) in response to external stimuli, which is called synaptic plasticity (Abbott and Nelson, 2000). Artificial synaptic devices that can emulate the synaptic plasticity are, therefore, a key building block for a neuromorphic computing system. A simple yet energy-efficient synaptic device is the memristor, whose resistance can be continuously tuned depending on the history of electrical signals (Chang et al., 2011; Ohno et al., 2011). Most reported memristors are based on filament-forming oxides (Yan et al., 2018; Guan et al., 2019), electrolyte-gated oxides and polymers (Ge et al., 2019; Gkoupidenis et al., 2015), two-dimensional (2D) nitrides and sulfides (Shi et al., 2017; Wang et al., 2018; Li et al., 2018), and phase change materials (Tuma et al., 2016; Kuzum et al., 2012; Ge et al., 2020). These memristors operate through the migration and ordering of ions or atoms, which are inherently stochastic and difficult to control (Burr et al., 2018). Large device variability and poor reliability are therefore ubiquitous in these memristors.

A promising alternative to the aforementioned memristors is the ferroelectric synapse, whose synaptic behavior is induced by a purely electronic switching process, namely, polarization switching. There have been two types of ferroelectric synapses demonstrated so far: ferroelectric tunnel junctions (FTJs) (Chanthbouala et al., 2012; Wen et al., 2014; Li et al., 2019; Majumdar et al., 2019; Boyn et al., 2017; Guo et al., 2018;

[1]Institute for Advanced Materials, South China Academy of Advanced Optoelectronics, South China Normal University, Guangzhou 510006, China

[2]Guangdong Provincial Key Laboratory of Optical Information Materials and Technology, South China Academy of Advanced Optoelectronics, South China Normal University, Guangzhou 510006, China

[3]Department of Industrial Systems Engineering and Management, National University of Singapore, 117576, Singapore

[4]National Center for International Research on Green Optoelectronics, South China Normal University, Guangzhou 510006, China

[5]School of Materials Science and Engineering, Nanjing University of Science and Technology, Nanjing 210094, China

[6]Laboratory of Solid State Microstructures and Innovation Center of Advanced Microstructures, Nanjing University, Nanjing 210093, China

[7]Lead Contact

*Correspondence: fanzhen@m.scnu.edu.cn

https://doi.org/10.1016/j.isci.2020.101874

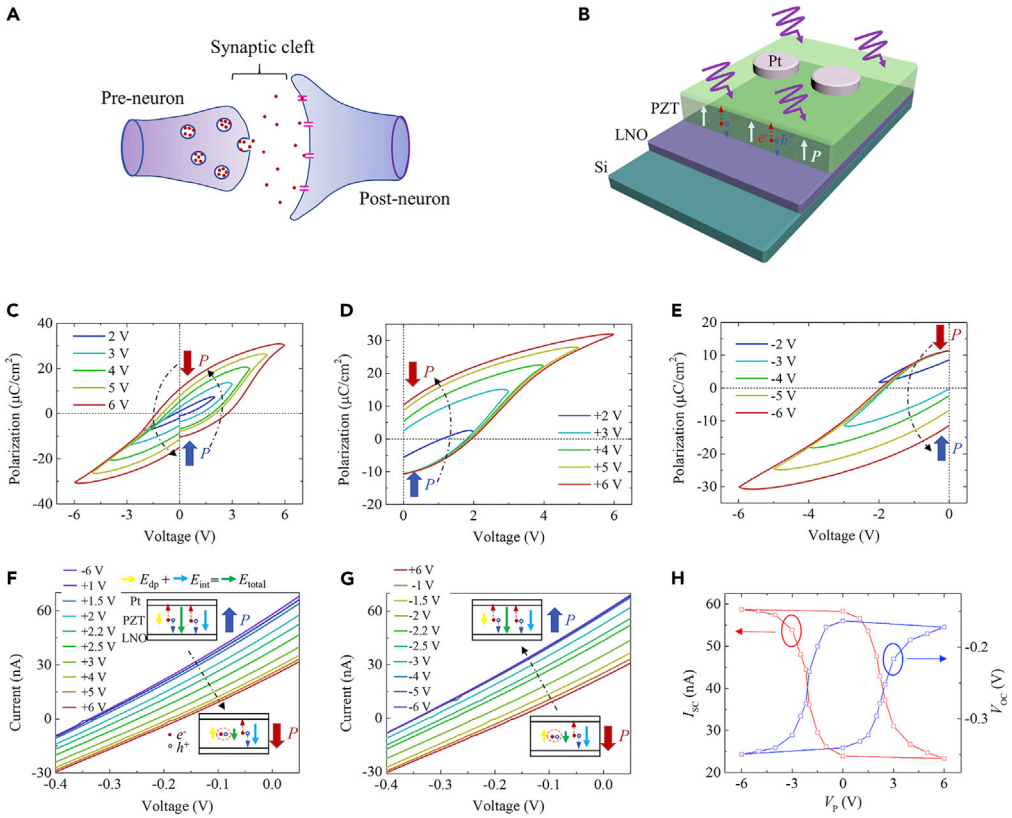

Figure 1. Polarization-Modulated Photovoltaic Response in the FePV Device

(A and B) Schematic illustrations of the structures of (A) a biological synapse and (B) a Pt/PZT/LNO FePV device grown on a silicon substrate.

(C–G) (C) Bipolar, (D) positive monopolar, and (E) negative monopolar *P-V* hysteresis loops measured with different applied voltages (frequency: 3.3 kHz). Illuminated *I-V* characteristics measured after applying (F) positive pulses from +1 V to +6 V (starting from the initial −6-V pulse-written state) and (G) negative pulses from −1 V to −6 V (starting from the initial +6-V pulse-written state). Insets in (F) and (G) show the variation of E_{total} (vector sum of E_{dp} and E_{int}) during the polarization switching.

(H) Evolutions of I_{SC} and V_{OC} as a function of pulse amplitude (V_p).

Chen et al., 2018; Ma et al., 2020) and ferroelectric field effect transistors (FeFETs) (Hoffman et al., 2010; Nishitani et al., 2012; Tian et al., 2019; Kim and Lee, 2019; Luo et al., 2020), which use the switchable polarization to tune the tunneling current and channel current, respectively. Although both FTJs and FeFETs have shown large ON/OFF ratios, low energy dissipations, and synaptic functions including short-/long-term plasticity and spike-timing-dependent plasticity (STDP) (Li et al., 2019; Majumdar et al., 2019; Boyn et al., 2017; Guo et al., 2018; Chen et al., 2018; Nishitani et al., 2012; Tian et al., 2019), they are still facing challenges in terms of the controllability of polarization and the device fabrication. Specifically, an FTJ requires the ferroelectric film to be ultra-thin (several nanometers) to allow the current tunneling, whereas an FeFET needs to use a semiconductor channel whose screening ability is apparently lower than that of a metal electrode. Both ultra-small film thickness (Kohlstedt et al., 2005; Cai et al., 2011) and poor screening at the ferroelectric/semiconductor interface (Wurfel et al., 1973) can lead to a large depolarization field (E_{dp}). The large E_{dp} in turn causes the polarization instability, making it difficult to precisely control the polarization state and associated conductance level. In addition, an FTJ typically requires strained epitaxy of an ultra-thin ferroelectric film on a single-crystalline oxide substrate (Chanthbouala et al., 2012; Wen et al., 2014; Li et al., 2019; Majumdar et al., 2019; Boyn et al., 2017; Guo et al., 2018), whereas for an FeFET a careful optimization of the ferroelectric/semiconductor interface quality is demanded (Hoffman et al., 2010; Nishitani et al., 2012; Tian et al., 2019; Kim and Lee, 2019). The limited polarization controllability as well as complex and costly fabrication processes may, therefore, become the major challenges for both FTJs and FeFETs to be used as synaptic devices in hardware-based neural networks.

To address the above-mentioned challenges, ferroelectric synapses with a new way to read out the polarization state, other than the tunneling current in FTJs and the channel current in FeFETs, should be explored. Ferroelectric photovoltaic (FePV) effect offers a viable way of readout, i.e., polarization-controlled switchable photocurrent (Yuan et al., 2014; Fan et al., 2015; Ji et al., 2010; Yi et al., 2011; Guo et al., 2013). Using the photocurrent as the readout, ferroelectric materials (in any form and with a broad range of thicknesses) (Tan et al., 2018, 2019; Yang et al., 2010; Qin et al., 2009; Chen et al., 2011; Bai et al., 2018; He et al., 2019; Blouzon et al., 2016; Alexe and Hesse, 2011) sandwiched between two metal electrodes can in principle function as FePV synapses. Therefore, the limitations in FTJs (ultra-small film thickness and epitaxial growth) and FeFETs (semiconductor channel and optimization of interface quality) no longer exist in the FePV synapses. One consequence is that the E_{dp} effect can be reduced in the FePV synapses and hence the controllability of polarization is enhanced, beneficial for the performance of neural networks built from these devices. Another consequence is that the FePV synapses with simple structures can be fabricated using a wide variety of low-cost techniques and substrates. These advantages suggest the immense application potential of FePV synapses in neuromorphic computing architectures. It is, however, noted that whereas the FePV effect was once used for the binary data storage (Guo et al., 2013), the use of the FePV effect for synaptic applications has never been attempted yet.

Herein, we develop a proof-of-concept FePV synapse with a simple two-terminal structure of Pt/$Pb(Zr_{0.2}Ti_{0.8})O_3$ (PZT)/$LaNiO_3$ (LNO) (Figure 1B). PZT with a Zr/Ti ratio of 20/80 is chosen as the FePV material because it possesses robust ferroelectricity, strong photoresponse in the UV wavelength region (Tan et al., 2019), and wide process window. The Pt/PZT/LNO FePV device can be facilely grown on a silicon substrate, showing its good compatibility with the silicon technology. More importantly, it exhibits gradual polarization switching behavior benefitting from the multi-domain switching with relatively slow dynamics in the polycrystalline PZT film. This gives rise to multilevel nonvolatile photovoltaic responses, which can be continuously tuned with small nonlinearity and write noise, highlighting the good controllability. Using the photovoltaic response as the synaptic weight, the FePV device exhibits various synaptic functions, such as long-term potentiation (LTP), long-term depression (LTD), and STDP. A FePV synapse-based neural network is further simulated, and it achieves high accuracies (>93%) for image recognition, comparable to those achieved by neural networks based on high-quality FTJs and FeFETs. These highly controllable and silicon-compatible FePV synapses are therefore a promising candidate for synaptic applications.

RESULTS AND DISCUSSION

Gradual Polarization Switching in Polycrystalline PZT Film

The key component of the proposed FePV synapse is the polycrystalline PZT film (Figure S1) exhibiting gradual polarization switching, which enables the access to multilevel photovoltaic responses. The polarization switching behavior was first investigated by measuring bipolar and monopolar polarization-voltage (*P-V*) hysteresis loops. Figure 1C shows that the bipolar *P-V* loop opens gradually as the amplitude of applied voltage increases. The remanent polarization (P_r) can reach ~10 μC/cm^2, consistent with that reported for polycrystalline PZT (Meng et al., 2000). In addition, these bipolar *P-V* loops have a slanted shape, indicative of gradual polarization switching. The monopolar *P-V* loops, shown in Figures 1D and 1E, further illustrate that the polarization is gradually switched to the downward (upward) direction as the amplitude of applied positive (negative) voltage increases.

Gradual Polarization Switching-Induced Multilevel Photovoltaic Responses

To investigate the effect of gradual polarization switching on the photovoltaic response, current-voltage (*I-V*) characteristics under illumination were measured for the FePV device in different polarization states. UV light with a wavelength of 365 nm and an intensity of 105 mW/cm^2 was used for illumination (Figure S2). The polarization was first set in the fully upward (downward) state by applying a −6 V (+6 V) write pulse with a width of 1 ms. Then, a series of positive (negative) write pulses with increasing amplitudes (pulse width: 10 μs) was applied sequentially to produce intermediate polarization states. No erase pulses were applied between these write pulses. In each intermediate polarization state, the illuminated *I-V* characteristics were measured with a sufficiently low voltage sweeping speed (Figure S3A). The dark *I-V* characteristics were also measured, and the dark currents at low voltages were found to be orders of magnitude smaller than the photocurrent (Figure S3B). The applied voltage is defined to be positive when the top electrode is positively biased, and the current is termed positive when it flows from top to bottom.

As shown in Figure 1F, the FePV device exhibits noticeable photovoltaic behavior with a short-circuit current (I_{SC}) of ~57 nA and an open-circuit voltage (V_{OC}) of ~ -0.33 V in the fully upward polarization state (i.e., the −6-V pulse-written state). Starting from this state, applying positive write pulses from +1 V to +6 V leads to the successive shift of the illuminated *I-V* curve toward the origin, indicating the continuous decrease of photovoltaic response. Eventually, I_{SC} and V_{OC} decrease to ~23 nA and ~-0.15 V, respectively, in the fully downward polarization state (i.e., the +6-V pulse-written state). All the available photovoltaic responses are rather stable against time (Figure S4), attesting to the nonvolatility of the emerging intermediate photoresponsive states. On the contrary, applying negative write pulses from −1 V to −6 V leads to the successive shift of the illuminated *I-V* curve away from the origin (Figure 1G). Moreover, the values of I_{SC} and V_{OC} are almost recovered to those in the initial −6-V pulse-written state (see comparison between Figures 1F and 1G). Figure 1H presents the evolutions of I_{SC} and V_{OC} as a function of write pulse amplitude, both of which form well-shaped hysteresis loops akin to the *P-V* hysteresis loops. Similar successive shift of the illuminated *I-V* curve and hysteretic evolutions of I_{SC} and V_{OC} with applied write pulse are observed at different light intensities (Figures S5 and S6). Apparently, the observed reversible multilevel modulation of photovoltaic response is associated with the gradual polarization switching in the polycrystalline PZT film (Figures 1C–1E). Notably, if the polarization switching is abrupt, only two bistable photoresponsive states can commonly be accessed, as observed in epitaxial ferroelectric films (Figure S7).

The modulation of photovoltaic response by polarization is further confirmed by microscopic observations of concurrent changes in domain configuration and photocurrent (Figures S8 and S9). The mechanism of how the polarization controls the photovoltaic response in our FePV device is discussed in detail with Figure S10. Briefly, a switchable E_{dp} and an unswitchable internal bias field (E_{int}) may be considered as the driving forces for the photovoltaic effect (Ji et al., 2010; Fan et al., 2017a). In the fully upward polarization state, both E_{dp} and E_{int} are oriented downward, resulting in a large total field (E_{total}) pointing downward (inset in Figure 1F). When the polarization is switched downward, E_{dp} rotates to the upward direction, whereas E_{int} remains unchanged (inset in Figure 1F). Given that $|E_{int}|$ is larger than $|E_{dp}|$, the resultant E_{total} is still pointing downward but its magnitude is smaller than that in the fully upward polarization state. As a result, the magnitudes of I_{SC} and V_{OC} decrease (increase), whereas their signs remain unchanged as the polarization switches from upward to downward (downward to upward) (Figures 1F and 1G). As the gradual polarization switching induces a dynamic modulation of E_{total}, multilevel photovoltaic responses are thus produced.

Domain Dynamics Underlying Gradual Polarization Switching

Because the gradual polarization switching is crucial for realizing continuously tunable photovoltaic response, further understanding of the underlying domain dynamics is required. Figure 2A shows the evolution of domain configuration in the polycrystalline PZT film with varying write voltage, measured by piezoresponse force microscopy (PFM). As the write voltage increases from +1 V to +4 V, the purple areas with downward domains gradually expand, whereas the yellow areas with upward domains gradually shrink. Opposite domain evolution is observed as the write voltage varies from −1 V to −4 V. Interestingly, the plot of area percentage of upward domains against write voltage forms a hysteresis loop (Figure 2B), akin to the *P-V* hysteresis loops (Figure 1C). These PFM imaging results therefore directly reveal the continuous domain evolution behavior at the microscopic level. The continuous domain evolution is attributed to the fact that the polycrystalline PZT film possesses multi-domains with small sizes (minimum size of an individual domain is below ~100 nm) facilitating the formation of multiple nonvolatile domain configurations during the domain switching.

To gain deeper insights into the domain dynamics, switchable polarizations (ΔP) as a function of pulse amplitude and width were measured using a positive-up-negative-down (PUND) method (Schloss and McIntyre, 2003; Borkar et al., 2017). In the PUND method, the first and second pulses with the same polarity measure the total polarization (P_{total}) and nonswitchable polarization (P_{ns}), respectively. ΔP is obtained by subtracting P_{ns} from P_{total}. Figure 2C displays that the normalized ΔP (ΔP_{norm}) systematically increases with increasing pulse amplitude at a given pulse width or with increasing pulse width at a given pulse amplitude. This indicates that the domains take a longer (shorter) time to be switched at a lower (higher) electric field. To quantitatively describe the switching kinetics, the nucleation-limited switching (NLS) model (Jo et al., 2007; Tagantsev et al., 2002) was employed. In this model, domain switching occurs region by region independently, and the switching in each region is governed by the nucleation of reversed domain. The time-dependent ΔP can be expressed as:

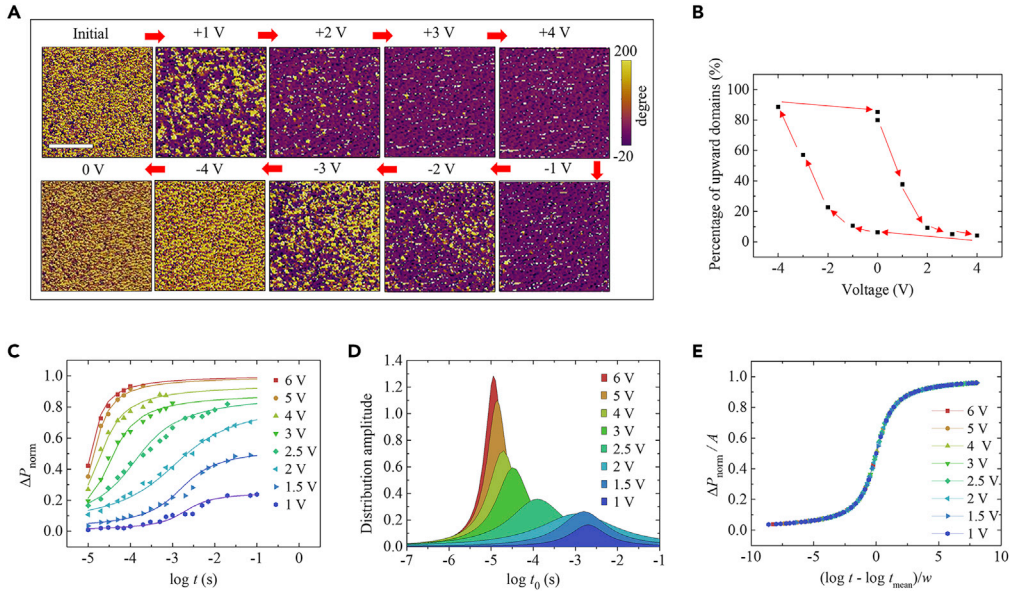

Figure 2. Domain Switching Kinetics in the Polycrystalline PZT Film

(A) PFM phase images measured on the bare PZT film after applying different write voltages (varying as 0 → +4 V → −4 V → 0). Scale bar, 1 μm.

(B) Area percentage of upward domains as a function of write voltage, as statistically obtained from (A).

(C) Normalized switchable polarization (ΔP_{norm}) versus pulse width under different pulse amplitudes measured using the PUND method.

(D) Lorentzian distributions of characteristic switching times (t_0) extracted from the fits in (C).

(E) Rescaled ΔP_{norm} ($\Delta P_{norm}/A$) as a function of pulse width using the parameters for the NLS model.

$$\Delta P(t) = 2P_s \int_{-\infty}^{\infty} \left[1 - \exp\{-(t/t_0)^n\}\right] F(\log t_0) d(\log t_0) \qquad \text{(Equation 1)}$$

where P_s is the spontaneous polarization ($\Delta P/2P_s$ is indeed ΔP_{norm}), t_0 is the characteristic switching time, n is the effective dimension ($n = 2$ for thin films, Jo et al., 2007), and $F(\log t_0)$ is Lorentzian distribution of the logarithm of switching times. The expression of $F(\log t_0)$ is given by:

$$F(\log t_0) = \frac{A}{\pi}\left[\frac{w}{(\log t_0 - \log t_{mean})^2 + w^2}\right] \qquad \text{(Equation 2)}$$

where A is an amplitude factor, t_{mean} is the mean switching time (i.e., the center of the distribution curve peak), and w is the half-width at half-maximum of the distribution curve peak.

As shown in Figure 2C, the experimental data of $\Delta P_{norm}(t)$ can be well fitted by the NLS model. Figure 2D presents the Lorentzian distribution curves at different pulse amplitudes. As the pulse amplitude increases, the distribution curve peak shifts leftward and becomes sharper, corresponding to the decreases of t_{mean} and w, respectively. t_{mean} decreases from $\sim 10^{-3}$ to $\sim 10^{-5}$ s as pulse amplitude increases from 1 to 6 V (corresponding to 50 to 300 kV/cm). These t_{mean} values are at least one order of magnitude larger than those in epitaxial ferroelectric films in the same electric field range (So et al., 2005), well accounting for the gradual feature of polarization switching in our polycrystalline PZT film.

By rescaling the $\Delta P_{norm}(t)$ data using $(\log t - \log t_{mean})/w$, all the curves merge into a single arctangent curve (Figure 2E). This scaling behavior suggests that the switching times obey the Lorentzian distribution. Moreover, the dependence of the mean switching time t_{mean} on the reciprocal of electric field follows the Merz's law (Jo et al., 2007) (Figure S11). These results in turn validate the NLS model. Therefore, the nucleation-limited multi-domain switching with relatively slow dynamics gives rise to the gradual polarization switching in our polycrystalline PZT film.

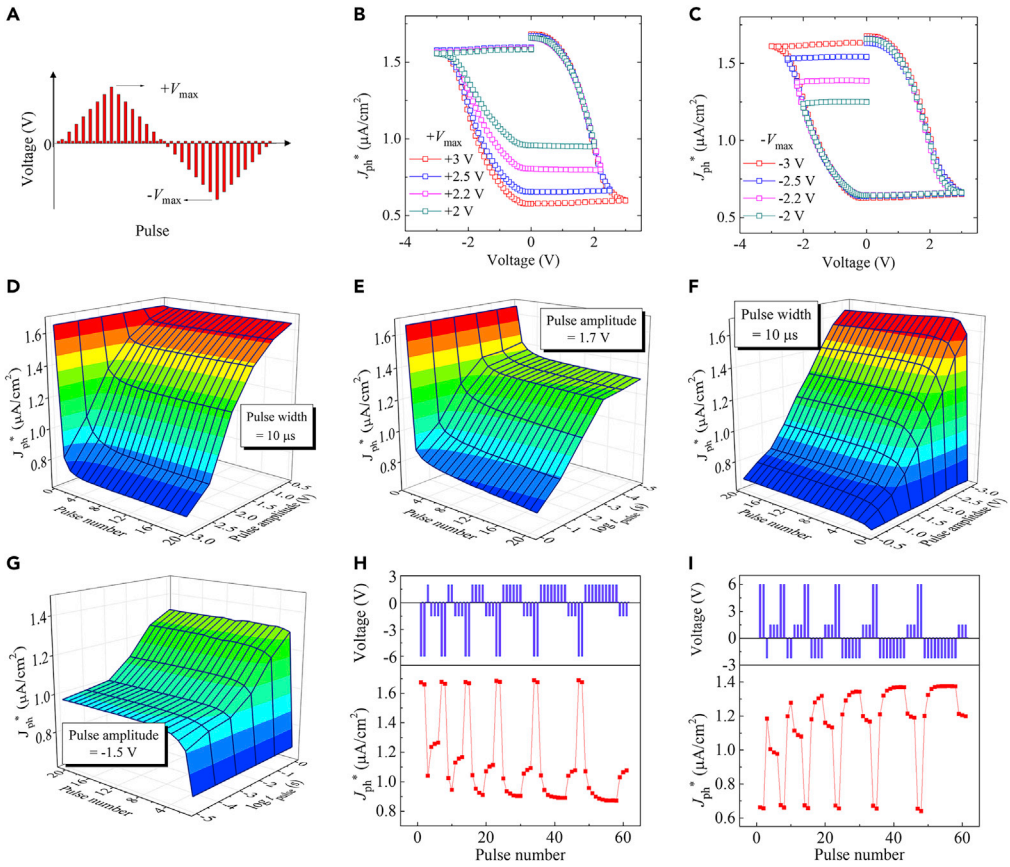

Figure 3. Continuously Tunable Photovoltaic Response (J_{ph}*) in the FePV Synapse

(A–G) (A) A schematic showing the pulse train following a triangular profile. Dependences of J_{ph}* on the pulse amplitude measured using the pulse trains (shown in A) with varying (B) $+V_{max}$ and (C) $-V_{max}$. Evolutions of J_{ph}* measured using repeated pulses with (D and F) varying pulse number and pulse amplitude while fixing the pulse width and (E and G) varying pulse number and pulse width while fixing the pulse amplitude.

(H) Evolution of J_{ph}* (lower panel) measured using the negative-positive-negative pulse train (upper panel) where the number of positive pulses (+2.2 V) between two negative pulse groups is varied.

(I) Evolution of J_{ph}* (lower panel) measured using the positive-negative-positive pulse train (upper panel) where the number of negative pulses (−2.2 V) between two positive pulse groups is varied.

Modulation of Photovoltaic Response by Electrical Pulse

With the aforementioned understandings, the gradual polarization switching-induced multilevel photovoltaic responses in the FePV device were further characterized. The photocurrent density at 0 V per unit light intensity, denoted by J_{ph}* with the superscript "*" meaning "per 1 mW/cm^2," was used as a quantitative term to represent the photovoltaic response. Note that the J_{ph}* data presented hereafter were measured at a light intensity of 105 mW/cm^2 and those measured at other light intensities are shown in Figures S12 and S13.

Figures 3B and 3C show the hysteretic evolutions of J_{ph}* as the pulse amplitude varies following triangular profiles (see Figure 3A) while keeping the pulse width at 1 ms. Starting from the same state written by the −6-V pulse, applications of positive pulse trains with maximum amplitudes of +2, +2.2, +2.5, and +3 V result in intermediate J_{ph}* levels of ~0.95, ~0.80, ~0.66, and ~0.60 μA/cm^2, respectively (Figure 3B). Likewise, intermediate J_{ph}* levels ranging from ~1.24 to ~1.38, ~1.54, and ~1.62 μA/cm^2 can be obtained by applying negative pulse trains with maximum amplitudes increasing from −2 to −2.2, −2.5, and −3 V, respectively. All these intermediate J_{ph}* levels are nonvolatile based on the observations of almost flat bottom and top parts of the hysteresis loops (Figures 3B and 3C).

Besides the triangular pulse trains, repeated pulses were also used to tune the polarization states and consequent J_{ph}* levels. As shown in Figures 3D and 3E, the initially set high J_{ph}* decreases and eventually

reaches a saturated value as the number of applied positive pulses increases. The saturation of J_{ph}* can be explained by the fact that the domains that are responsive under this pulse amplitude and width are switched during the first few pulses and then no more domains can be switched with further increasing pulse number. In addition, the variation of J_{ph}* from the initial value to the saturated value becomes larger with larger pulse amplitude and longer pulse duration, due to the switching of more domains. Similar dependences of the J_{ph}* variation on pulse amplitude and width are observed when tuning the initial low-J_{ph}* state by applying repeated negative pulses (Figures 3F and 3G).

Then, the effects of the history of applied pulses on J_{ph}* were investigated by applying consecutive pulse trains containing alternate positive and negative pulses. Figure 3H (upper panel) shows the sequence of a negative-positive-negative pulse train: two −6-V pulses (for setting the high-J_{ph}* state), +2.2-V pulses with varied numbers, and three −1.5-V pulses (the widths of all pulses are 1 ms). Applying this pulse train to the FePV device produces the evolution of J_{ph}* shown in Figure 3H (lower panel). Interestingly, the J_{ph}* value after each group of −1.5-V pulses gradually decreases, which can be attributed to the increasing number of previously applied +2.2-V pulses. Similar history dependence of the J_{ph}* variation is also observed when applying a positive-negative-positive pulse train (Figure 3I).

Synaptic Functions of the FePV Synapse

Because the FePV device exhibits continuous modulation of J_{ph}* depending on the amplitude, duration, and history of applied pulses, it can thus be qualified as a synaptic device with the tunable photovoltaic response (i.e., J_{ph}*) corresponding to the synaptic weight. To further demonstrate the synaptic plasticity of the FePV device, the STDP behavior was characterized, as shown in Figure S14. In addition, LTP and LTD characteristics were also measured using an increasing-voltage pulse scheme (upper panel of Figure 4A). In this pulse scheme, a positive pulse train (amplitude: from 0 to +2.5 V in increments of ~0.17 V; width: 10 μs) and a negative pulse train (amplitude: from 0 to −2.5 V in decrements of ~ -0.17 V; width: 10 μs) were applied alternately, and J_{ph}* was measured after each pulse. The reason for using this pulse scheme was because more domains become responsive and can be switched under larger pulse amplitude, thus allowing a continuously tuned photocurrent with increasing pulse number.

As shown in Figure 4A, J_{ph}* gradually decreases as the number of positive pulses increases, indicating an LTD behavior. Conversely, the LTP behavior, manifesting as the increase of J_{ph}*, occurs during the application of the negative pulse train. These results are consistent with those in Figures 1 and 3, all of which can be explained by the polarization modulation of photovoltaic response. Almost identical LTD and LTP processes can be repeated for 20 cycles, demonstrating a small cycle-to-cycle variation (~2%). In addition, there are 16 different J_{ph}* levels in the LTD and LTP processes, confirming that multiple photoresponsive states are accessible.

FePV Synapse-Based Neural Network

Using the experimentally measured cyclic LTP/LTD characteristics to map the synaptic weights, we further simulated a FePV synapse-based neural network for image recognition (Figures 4B and 4C). A three-layer (one hidden layer) neural network, as shown in Figure 4B, was used for the back-propagation algorithm-based simulations (Saerens and Soquet, 1991; Hegazy et al., 1994). Each synaptic weight matrix between two neuron layers was modeled as a crossbar (Figure 4C). The crossbar performed vector-matrix multiply and parallel rank one outer product update, with our FePV devices acting as the synapses in the crossbar. The neural network was trained and tested on two datasets: a small image version (8 × 8 pixels) of handwritten digits from the "Optical Recognition of Handwritten Digits" dataset (Kang and P.-Brown, 2008) and a large image version (28 × 28 pixels) of handwritten digits from the "Modified National Institute of Standards and Technology" (MNIST) dataset (Deng, 2012). The pixel values of the images were encoded as the light intensities used to illuminate the FePV synapses (see Figure S15 for detailed descriptions about the operations of the FePV synapse-based neural network).

Generally, the performance of a neural network is greatly influenced by the controllability (e.g., nonlinearity and write noise) of synaptic devices, which can be quantitatively analyzed using the probability distribution of the change in J_{ph}* induced by a write operation (i.e., ΔJ_{ph}*). The plots of ΔJ_{ph}* versus initial J_{ph}* (i.e., $J_{ph}{}^*_0$), derived from the cyclic LTP/LTD characteristics, are presented in Figures 4D and 4E for potentiation and depression, respectively. The magnitude of ΔJ_{ph}* first increases and then decreases with increasing (decreasing) $J_{ph}{}^*_0$ in the potentiation (depression) process. The average slopes of ΔJ_{ph}* versus $J_{ph}{}^*_0$ are

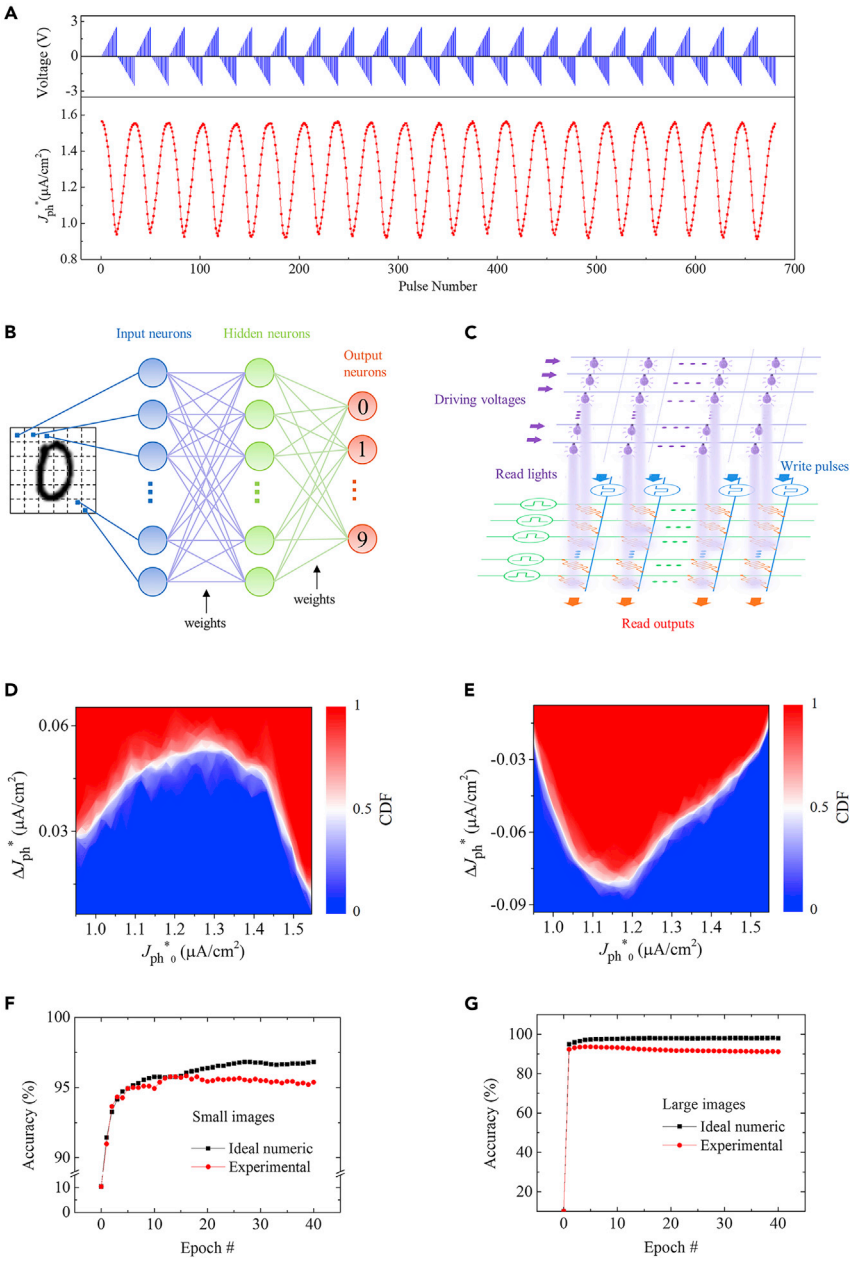

Figure 4. Long-Term Plasticity and Neural Network Simulation

(A) LTD and LTP characteristics (lower panel) measured using the alternate positive and negative pulse trains (upper panel).

(B) A schematic showing a three-layer (one hidden layer) neural network.

(C–G) (C) Schematics of a crossbar architecture based on the FePV synapses and the light arrays used for the read operation. Probability distributions of the change in J_{ph}* induced by a write operation (i.e., ΔJ_{ph}*) versus initial J_{ph}* (i.e., J_{ph}*$_0$) for (D) potentiation and (E) depression. CDF denotes the cumulative distribution function. Evolutions of accuracies with training epochs achieved by the ideal floating-point-based and the FePV synapse-based neural networks for recognizing (F) small (8 × 8 pixels) and (G) large (28 × 28 pixels) images.

~0.12 and ~0.21 for potentiation and depression, respectively, which are relatively small and thus demonstrate the small nonlinearity of our FePV synapses (note that a slope of zero means that the synaptic device is ideally linear). In addition, ΔJ_{ph}* deviates with an average standard deviation (σ_S) of 4.75 × 10^{-3} μA/cm^2 (4.96 × 10^{-3} μA/cm^2) for potentiation (depression). The average signal-to-noise ratios $\Delta J_{ph}^{*2}/\sigma_S^2$ are ~80

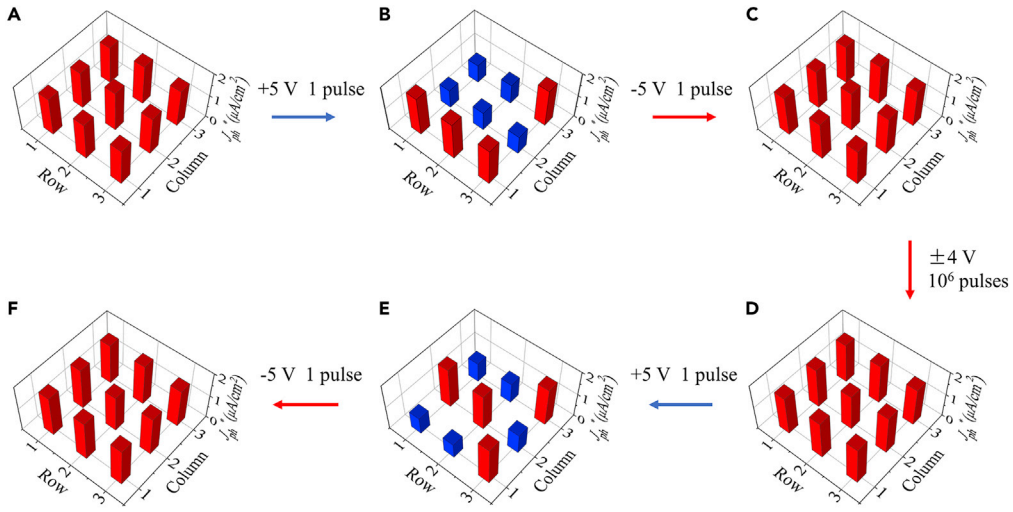

Figure 5. Device-to-Device Variation and Endurance

(A) A 3 × 3 FePV synapse array with uniformly high J_{ph}* values in the initial state.

(B and C) Distribution of J_{ph}* values after applying (B) +5-V and (C) −5-V pulses to each of the five selected FePV synapses (forming a letter "P").

(D) The cyclic switching of all FePV synapses by applying ±4-V pulses repeatedly for 10^6 cycles.

(E and F) Distribution of J_{ph}* values after applying (E) +5-V and (F) −5-V pulses to each of other five selected FePV synapses (forming a letter "V").

and ~127 for potentiation and depression, respectively, which are quite large and comparable to those observed in the state-of-the-art Li-ion synaptic transistors (Fuller et al., 2017). The small nonlinearity and write noise of our FePV synapses may render good performance for the neural network.

Figures 4F and 4G show the recognition accuracies of the FePV synapse-based neural network after training with small and large images, respectively. The results of the ideal floating-point-based neural network are also shown, which represent the theoretical limits for the neuromorphic algorithm. For small images, the accuracy exceeds 90% after the first two training epochs and approaches ~95.4% after 40 training epochs, which is only ~1.4% lower than the ideal accuracy (~96.8%). For large images, the accuracy reaches a maximum value of ~93.7% after 4 training epochs, which deviates the ideal accuracy (~98.0%) by ~4.3%. Further increasing the training epoch leads to the decrease of accuracy, probably due to the issue of over-fitting. Nevertheless, these accuracies rank high among those obtained with FTJs (Li et al., 2019; Ma et al., 2020), FeFETs (Yang et al., 2018a; Kim and Lee, 2019), filament-forming oxides (Choi et al., 2018), and phase change materials (Ge et al., 2019, 2020) (see Table S1 for details), demonstrating the great potential of FePV synapses for application in high-performance neuromorphic computing. Note that in the above simulations the simulated accuracy already took into account the effect of the cycle-to-cycle variation because the cyclic LTP/LTD characteristics were used. The effects of other non-ideal factors of the FePV synapses on the simulated accuracy can be found in Figure S16.

Reliability and Energy Consumption of the FePV Synapse

For a neural network, besides the accuracy, the reliability is also a key concern. While the cycle-to-cycle variation and retention of the constituent synaptic devices have already been addressed, the device-to-device variation and endurance are yet to be measured. Measurements on the device-to-device variation and endurance were performed with an array of 3 × 3 separated FePV synapses, as shown in Figure 5. In the initial state (Figure 5A), the J_{ph}* values of all FePV synapses are distributed uniformly at ~1.65 μA/cm^2. After applying a +5-V pulse (10 μs) to each of five selected FePV synapses (forming a letter "P"), the J_{ph}* values of these devices decrease uniformly to ~0.81 μA/cm^2 (Figure 5B). The J_{ph}* values can be recovered to ~1.65 μA/cm^2 by simply applying a −5-V pulse (10 μs) to each of the selected FePV synapses (Figure 5C). All the FePV synapses were then switched by ±4-V pulses repeatedly for 10^6 cycles (note: the pulse amplitude was selected to be ~1.5 times the coercive voltage, following the standard protocol used for the endurance test). Afterward, the pulse modulations of the J_{ph}* values of other five selected FePV synapses

(forming a letter "V") were demonstrated, and the J_{ph}* variations were observed to be similar to those before the endurance test, as shown in Figures 5D–5F. Detailed evolutions of polarization and J_{ph}* with the number of switching cycles are presented in Figure S17, revealing that both polarization and J_{ph}* change slightly even after switching for 10^6 cycles. These results demonstrate that our FePV synapses have small device-to-device variation and good endurance.

The last concern is the energy consumption. For the FePV synapse presented in this work, the write energy is calculated to be on the order of ~10 nJ (Figure S18), which is much higher than the fJ level as reported previously (Ma et al., 2020; Tian et al., 2019). The reasons for the high write energy include the large device area (3.14×10^{-4} cm^2) and large pulse width (≥ 10 μs). Indeed, we previously demonstrated that the switchable photovoltaic response could be observed in an FePV device as small as ~1 $μm^2$ (Fan et al., 2017b). In addition, as indicated by Figure 2C, to switch the same amount of polarization, a small increase in the pulse amplitude can lead to a decrease of the pulse width by orders of magnitude. For example, a 12.3-V pulse can switch a polarization of ~134 $μC/cm^2$ within a switching time of 1.7 ns, and the triggered current density was $\sim 9 \times 10^4$ A/cm^2 (Grigoriev et al., 2011). For our PZT film with a switchable polarization of ~20 $μC/cm^2$, the current density triggered by the 12.3-V/1.7-ns pulse may thus be $\sim 1.3 \times 10^4$ A/cm^2. Therefore, the write energy of our FePV synapse may be reduced to ~2.7 pJ ($12.3\ V \times 1.3 \times 10^4\ A/cm^2 \times 1\ μm^2 \times 1.7$ ns). In terms of the read energy, only the light energy is considered because the photocurrent exists at zero read voltage. Using the light intensity of 105 mW/cm^2 and the device area of 3.14×10^{-4} cm^2, the light power is calculated as ~0.03 mW. Although in this work the pulsed light was not used, it was reported that the FePV effect could occur by applying light pulses as short as ~1 ns (Xing et al., 2015; Yang et al., 2020; Li et al., 2017; Gerasimenko et al., 2019). Also considering the device downscaling (assuming a device area of ~1 $μm^2$), it is therefore possible to bring the read energy of the FePV synapse to ~1 aJ ($105\ mW/cm^2 \times 1\ μm^2 \times 1$ ns).

Merits of the FePV Synapse

Finally, let us summarize the merits of the FePV devices as artificial synapses. Unlike the traditional memristive devices, which are defect-mediated, the FePV devices use the polarization to modulate the photovoltaic response, thus providing a more precise control over the synaptic weight. Compared with other ferroelectric synapses, like FTJs and FeFETs, the FePV synapses have two major advantages as follows. First, the FePV synapses have simple structures and facile fabrication procedures. Taking our FePV synapse as an example, it consists of a simple two-terminal Pt/PZT (polycrystalline film)/LNO structure, which can be easily grown on a silicon substrate, demonstrating its good compatibility with the silicon technology. More generally, ferroelectric materials in any form (thin films, Tan et al., 2018; Yang et al., 2010; Tan et al., 2019; Qin et al., 2009; Chen et al., 2011; ceramics, Bai et al., 2018; He et al., 2019; single crystals, Blouzon et al., 2016; Alexe et al., 2011; etc.) can be used for constructing FePV synapses because of the universality of the FePV effect. By contrast, FTJs and FeFETs typically require the epitaxy growth (Chen et al., 2018; Ma et al., 2020) and careful optimization of the ferroelectric/semiconductor interface quality (Hoffman et al., 2010), respectively, and some of them are difficult to be integrated with the silicon substrate. The second advantage of the FePV synapses is the ability to directly measure and precisely control the polarization. As a result, the coupling between polarization and photovoltaic response can be unambiguously demonstrated, which not only makes clear the mechanism of the polarization-mediated synaptic behavior but also allows us to better control the synaptic weight. However, the direct measurement and precise control of polarization are still challenging for both FTJs (Boyn et al., 2017) and FeFETs (Tian et al., 2019), because of the ultra-thin ferroelectric films and semiconductor channels used in FTJs and FeFETs, respectively.

CONCLUSIONS

To sum up, we have proposed and demonstrated a prototype FePV synapse based on a polycrystalline PZT film sandwiched between Pt and LNO electrodes grown on a silicon substrate. This device relies on (1) the gradual polarization switching benefitting from the multi-domain switching with relatively slow dynamics and (2) the polarization control of photovoltaic effect, to achieve multilevel nonvolatile photovoltaic responses, as demonstrated by the combined *P-V* loop and PFM measurements. Moreover, the photovoltaic response (i.e., J_{ph}*) can be continuously and reversibly tuned by varying the amplitude, duration, and history of applied pulses, thus qualifying the FePV device as a synaptic device. Typical synaptic functions including LTP, LTD, and STDP have all been realized by the FePV synapses. More importantly, the FePV synapses also exhibit good controllability (small nonlinearity and write noise), high endurance, small device-to-device variation, and potentially low energy consumption. Consequently, a simulated neural

network built from these devices achieves a high accuracy of ~93.7% for recognizing the MNIST handwritten digits. Considering the above good performance as well as their simple fabrication and silicon compatibility, the FePV synapses may therefore represent a new type of hardware implementation of ferroelectric synapses for high-performance neuromorphic computing.

Limitations of the Study

The photocurrent of the present FePV device is at the 10-nA level, which can be further enhanced if a ferroelectric material with a narrower band gap is used. A quantitative relationship between the photocurrent response and the pulse parameters, which can guide us to design the pulse scheme, is yet to be established. Although the FePV synapse-based neural network has been simulated and good performance has been predicted, the hardware implementation is still challenging. This is mainly because the uses of increasing-voltage pulse scheme for small nonlinearity and light signals (John et al., 2020) for reading would increase the circuit complexity. Encoding the image pixel values as the light intensities increases the number of operation events.

Resource Availability

Lead Contact

Further information and requests for resources and reagents should be directed to and will be fulfilled by the Lead Contact, Prof. Zhen Fan (fanzhen@m.scnu.edu.cn).

Materials Availability

This study did not generate new unique materials.

Data and Code Availability

All data associated with the study are included in the paper and the Supplemental Information. Additional information is available from the Lead Contact upon reasonable request.

METHODS

All methods can be found in the accompanying Transparent Methods supplemental file.

SUPPLEMENTAL INFORMATION

Supplemental Information can be found online at https://doi.org/10.1016/j.isci.2020.101874.

ACKNOWLEDGMENTS

The authors would like to thank National Key Research Program of China (Nos. 2016YFA0201002 and 2016YFA300101), Science and Technology Program of Guangzhou (No. 2019050001), National Natural Science Foundation of China (Nos. 51790492, U1932125, 11674108, 51431006), Natural Science Foundation of Guangdong Province (No. 2020A1515010996). X.L. and Z.F. acknowledge the Project for Guangdong Province Universities and Colleges Pearl River Scholar Funded Scheme 2016 and 2018, respectively.

AUTHORS CONTRIBUTION

Z.F. conceived and planned the research. S.C. prepared the samples and measured the photovoltaic characteristics. J.R. and L.H. performed the neural network simulations. Q.H., R.T., M.Q., and G.Z. conducted XRD. Z.H., M.Z., and X.L. performed TEM. S.C., G.Y., and X.G. provided the AFM-based characterizations. All authors analyzed and discussed the experimental data. S.C., Z.F., G.Y., X.G., and J.-M.L. wrote and revised the manuscript.

DECLARATION OF INTERESTS

The authors declare no competing interests.

Received: July 29, 2020
Revised: September 29, 2020
Accepted: November 24, 2020
Published: December 18, 2020

REFERENCES

Abbott, L.F., and Nelson, S.B. (2000). Synaptic plasticity: taming the beast. Nat. Neurosci. *3*, 1178–1183.

Alexe, M., and Hesse, D. (2011). Tip-enhanced photovoltaic effects in bismuth ferrite. Nat. Commun. *2*, 256.

Bai, Y., Vats, G., Seidel, J., Jantunen, H., and Juuti, J. (2018). Boosting photovoltaic output of ferroelectric ceramics by optoelectric control of domains. Adv. Mater. *30*, 1803821.

Banerjee, W., Liu, Q., Lv, H.B., Long, S.B., and Liu, M. (2017). Electronic imitation of behavioral and psychological synaptic activities using TiO_x/Al_2O_3-based memristor devices. Nanoscale *9*, 14442–14450.

Blouzon, C., Chauleau, J.-Y., Mougin, A., Fusil, S., and Viret, M. (2016). Photovoltaic response around a unique 180° ferroelectric domain wall in single-crystalline $BiFeO_3$. Phys. Rev. B *94*, 094107.

Borkar, H., Rao, V., Tomar, M., Gupta, V., Scott, J.F., and Kumar, A. (2017). Experimental evidence of electronic polarization in a family of photo-ferroelectrics. RSC Adv. *7*, 12842–12855.

Boyn, S., Grollier, J., Lecerf, G., Xu, B., Locatelli, N., Fusil, S., Girod, S., Carrétéro, C., Garcia, K., Xavier, S., et al. (2017). Learning through ferroelectric domain dynamics in solid-state synapses. Nat. Commun. *8*, 14736.

Burr, G.W., Shelby, R.M., Sebastian, A., Kim, S., Kim, S., Sidler, S., Virwani, K., Ishii, M., Narayanan, P., Fumarola, A., et al. (2018). Neuromorphic computing using non-volatile memory. Adv. Phys. X *2*, 89–124.

Cai, M., Du, Y., and Huang, B. (2011). First-principles study of the critical thickness in asymmetric ferroelectric tunnel junctions. Appl. Phys. Lett. *98*, 102907.

Chang, T., Jo, S.H., and Lu, W. (2011). Short-term memory to long-term memory transition in a nanoscale memristor. ACS Nano *5*, 7669–7676.

Chanthbouala, A., Garcia, V., Cherifi, R.O., Bouzehouane, K., Fusil, S., Moya, X., Xavier, S., Yamada, H., Deranlot, C., Mathur, N.D., et al. (2012). A ferroelectric memristor. Nat. Mater. *11*, 860–864.

Chen, B., Li, M., Liu, Y., Zuo, Z., Zhuge, F., Zhan, Q.F., and Li, R.W. (2011). Effect of top electrodes on photovoltaic properties of polycrystalline $BiFeO_3$ based thin film capacitors. Nanotech *22*, 195201.

Chen, L., Wang, T.Y., Dai, Y.W., Cha, M.Y., Zhu, H., Sun, Q.Q., Ding, S.J., Zhou, P., Chua, L., and Zhang, D.W. (2018). Ultra-low power $Hf_{0.5}Zr_{0.5}O_2$ based ferroelectric tunnel junction synapses for hardware neural network applications. Nanoscale *10*, 15826–15833.

Choi, S., Tan, S.H., Li, Z., Kim, Y., Choi, C., Chen, P., Yeon, H., Yu, S., and Kim, J. (2018). SiGe epitaxial memory for neuromorphic computing with reproducible high performance based on engineered dislocations. Nat. Mater. *17*, 335–340.

Deng, L. (2012). The MNIST database of handwritten digit images for machine learning research. IEEE Signal Proc. Mag. *29*, 141–142.

Drachman, D.A. (2005). Do we have brain to spare? Neurology *64*, 2004–2005.

Eryilmaz, S.B., Kuzum, D., Yu, S., and Wong, H.S.P. (2015). Device and system level design considerations for analog-non-volatile-memory based neuromorphic architectures. In 2015 IEEE International Electron Devices Meeting (IEDM), pp. 4.1.1–4.14.

Fan, H., Chen, C., Fan, Z., Zhang, L., Tan, Z., Li, P., Huang, Z., Yao, J., Tian, G., Luo, Q., et al. (2017a). Resistive switching and photovoltaic effects in ferroelectric $BaTiO_3$-based capacitors with Ti and Pt top electrodes. Appl. Phys. Lett. *111*, 252901.

Fan, H., Fan, Z., Li, P., Zhang, F., Tian, G., Yao, J., Li, Z., Song, X., Chen, D., Han, B., et al. (2017b). Large electroresistance and tunable photovoltaic properties of ferroelectric nanoscale capacitors based on ultrathin super-tetragonal $BiFeO_3$ films. J. Mater. Chem. C *5*, 3323–3329.

Fan, Z., Sun, K., and Wang, J. (2015). Perovskites for photovoltaics: a combined review of organic–inorganic halide perovskites and ferroelectric oxide perovskites. J. Mater. Chem. A. *3*, 18809–18828.

Fuller, E.J., Gabaly, F.E., Léonard, F., Agarwal, S., Plimpton, S.J., Gedrim, R.B.J., James, C.D., Marinella, M.J., and Talin, A.A. (2017). Li-ion synaptic transistor for low power analog computing. Adv. Mater. *29*, 1604310.

Ge, C., Li, G., Zhou, Q.L., Du, J.Y., Guo, E.J., He, M., Wang, C., Yang, G.Z., and Jin, K.J. (2020). Gating-induced reversible H_xVO_2 phase transformations for neuromorphic computing. Nano Energy *67*, 104268.

Ge, C., Liu, C., Zhou, Q., Zhang, Q., Du, J., Li, J., Wang, C., Gu, L., Yang, G., and Jin, K. (2019). A ferrite synaptic transistor with topotactic transformation. Adv. Mater. *31*, 1900379.

Gerasimenko, Y.A., Karpov, P., Vaskivskyi, I., Brazovskii, S., and Mihailovic, D. (2019). Intertwined chiral charge orders and topological stabilization of the light-induced state of a prototypical transition metal dichalcogenide. Npj Quant. Mater. *4*, 32.

Gkoupidenis, P., Schaefer, N., Garlan, B., and Malliaras, G.G. (2015). Neuromorphic functions in PEDOT:PSS organic electrochemical transistors. Adv. Mater. *27*, 7176–7180.

Grigoriev, A., Azad, M.M., and McCampbell, J. (2011). Ultrafast electrical measurements of polarization dynamics in ferroelectric thin-film capacitors. Rev. Sci. Instrum. *82*, 124704.

Guan, Z., Yang, N., Ren, Z.Q., Zhong, N., Huang, R., Chen, W.X., Tian, B.B., Tang, X.D., Xiang, P.H., Duan, C.G., and Chu, J.H. (2019). Mediation in the second-order synaptic emulator with conductive atomic force microscopy. Nanoscale *11*, 8744–8751.

Guo, R., You, L., Zhou, Y., Lim, Z.S., Zou, X., Chen, L., Ramesh, R., and Wang, J. (2013). Non-volatile memory based on the ferroelectric photovoltaic effect. Nat. Commun. *4*, 1990.

Guo, R., Zhou, Y., Wu, L., Wang, Z., Lim, Z., Yan, X., Lin, W., Wang, H., Yoong, H.Y., Chen, S., et al. (2018). Control of synaptic plasticity learning of ferroelectric tunnel memristor by nanoscale interface engineering. ACS Appl. Mater. Inter. *10*, 12862–12869.

He, X., Chen, C., Li, C., Zeng, H., and Yi, Z. (2019). Ferroelectric, photoelectric, and photovoltaic performance of silver niobate ceramics. Adv. Funct. Mater. *29*, 1900918.

Hegazy, T., Fazio, P., and Moselhi, O. (1994). Developing practical neural network applications using back-propagation. Comput.-Aided Civil Infrastruct. Eng. *9*, 145–159.

Hoffman, J., Pan, X., Reiner, J.W., Walker, F.J., Han, J.P., Ahn, C.H., and Ma, T.P. (2010). Ferroelectric field effect transistors for memory applications. Adv. Mater. *22*, 2957–2961.

Ji, W., Yao, K., and Liang, Y.C. (2010). Bulk photovoltaic effect at visible wavelength in epitaxial ferroelectric $BiFeO_3$ thin films. Adv. Mater. *22*, 1763–1766.

Jo, J.Y., Han, H.S., Yoon, J.-G., Song, T.K., Kim, S.-H., and Noh, T.W. (2007). Domain switching kinetics in disordered ferroelectric thin films. Phys. Rev. Lett. *99*, 267602.

John, R.A., Acharya, J., Zhu, C., Surendran, A., Bose, S.K., Chaturvedi, A., Tiwari, N., Gao, Y., He, Y., Zhang, K.K., et al. (2020). Optogenetics inspired transition metal dichalcogenide neuristors for in-memory deep recurrent neural networks. Nat. Commun. *11*, 3211.

Kang, M., and P.-Brown, D. (2008). A modal learning adaptive function neural network applied to handwritten digit recognition. Inform. Sci. *178*, 3802–3812.

Kim, M.K., and Lee, J.S. (2019). Ferroelectric analog synaptic transistors. Nano Lett. *19*, 2044–2050.

Kohlstedt, H., Pertsev, N.A., Contreras, J.R., and Waser, R. (2005). Theoretical current-voltage characteristics of ferroelectric tunnel junctions. Phys. Rev. B *72*, 125341.

Kuzum, D., Jeyasingh, R.G.D., Lee, B., and Wong, H.S.P. (2012). Nanoelectronic programmable synapses based on phase change materials for brain-inspired computing. Nano Lett. *12*, 2179–2186.

Kuzum, D., Yu, S., and Wong, H.S.P. (2013). Synaptic electronics: materials, devices and applications. Nanotechnology *24*, 382001.

Li, D., Wu, B., Zhu, X., Wang, J., Ryu, B., Lu, W.D., Lu, W., and Liang, X. (2018). MoS_2 memristors exhibiting variable switching characteristics toward biorealistic synaptic emulation. ACS Nano *12*, 9240–9252.

Li, J., Ge, C., Du, J., Wang, C., Yang, G., and Jin, K. (2019). Reproducible ultrathin ferroelectric domain switching for high-performance neuromorphic computing. Adv. Mater. *32*, 1905764.

Li, J., Ge, C., Jin, K., Du, J., Yang, J., Lu, H., and Yang, G. (2017). Self-driven visible-blind photodetector based on ferroelectric perovskite oxides. App. Phys. Lett. *110*, 142901.

Luo, Z.D., Xia, X., Yang, M.M., Wilson, N.R., Gruverman, A., and Alexe, M. (2020). Artificial optoelectronic synapses based on ferroelectric field-effect enabled 2D transition metal dichalcogenide memristive transistors. ACS Nano *14*, 746–754.

Ma, C., Luo, Z., Huang, W., Zhao, L., Chen, Q., Lin, Y., Liu, X., Chen, Z., Liu, C., Sun, H., et al. (2020). Sub-nanosecond memristor based on ferroelectric tunnel junction. Nat. Commun. *11*, 1439.

Majumdar, S., Tan, H., Qin, Q.H., and van Dijken, S. (2019). Energy-efficient organic ferroelectric tunnel junction memristors for neuromorphic computing. Adv. Electron. Mater. *5*, 1800795.

Markram, H. (2012). The human brain Project. Sci. Am. *306*, 50–55.

Meng, X., Ma, Z., Sun, J., Bo, L., Ye, H., Guo, S., and Chu, J. (2000). Highly oriented $PbZr_{0.3}Ti_{0.7}O_3$ thin film on $LaNiO_3$-coated Si substrate derived from a chemical solution technique. Thin Solid Films *372*, 271–275.

Nishitani, Y., Kaneko, Y., Ueda, M., Morie, T., and Fujii, E. (2012). Three-terminal ferroelectric synapse device with concurrent learning function for artificial neural networks. J. Appl. Phys. *111*, 124108.

Ohno, T., Hasegawa, T., Tsuruoka, T., Terabe, K., Gimzewski, J.K., and Aono, M. (2011). Short-term plasticity and long-term potentiation mimicked in single inorganic synapses. Nat. Mater. *10*, 591–595.

Qin, M., Yao, K., and Liang, Y.C. (2009). Photovoltaic characteristics in polycrystalline and epitaxial $(Pb_{0.97}La_{0.03})(Zr_{0.52}Ti_{0.48})O_3$ ferroelectric thin films sandwiched between different top and bottom electrodes. J. Appl. Phys. *105*, 061624.

Saerens, M., and Soquet, A. (1991). Neural controller based on back-propagation algorithm. IEE Proc. F *138*, 55–62.

Schloss, L.F., and McIntyre, P.C. (2003). Polarization recovery of fatigued $Pb(Zr,Ti)O_3$ thin films: switching current studies. J. Appl. Phys. *93*, 1743–1747.

Shi, Y., Pan, C., Chen, V., Raghavan, N., Pey, K.L., Puglisi, F.M., Pop, E., Wong, H.S.P., and Lanza, M. (2017). Coexistence of volatile and non-volatile resistive switching in 2D h-BN based electronic synapses. In 2017 IEEE International Electron Devices Meeting (IEDM), pp. 5.4.1–5.4.4.

So, Y.W., Kim, D.J., Noh, T.W., Yoon, J.-G., and Song, T.K. (2005). Polarization switching kinetics of epitaxial $Pb(Zr_{0.4}Ti_{0.6})O_3$ thin films. Appl. Phys. Lett. *86*, 092905.

Tagantsev, A.K., Stolichnov, I., Setter, N., Cross, J.S., and Tsukada, M. (2002). Non-Kolmogorov-Avrami switching kinetics in ferroelectric thin films. Phys. Rev. B. *66*, 214109.

Tan, Z., Hong, L., Fan, Z., Tian, J., Zhang, L., Jiang, Y., Hou, Z., Chen, D., Qin, M., Zeng, M., et al. (2019). Thinning ferroelectric films for high-efficiency photovoltaics based on the Schottky barrier effect. NPG Asia Mater. *11*, 20.

Tan, Z., Tian, J., Fan, Z., Lu, Z., Zhang, L., Zheng, D., Wang, Y., Chen, D., Qin, M., Zeng, M., et al. (2018). Polarization imprint effects on the photovoltaic effect in $Pb(Zr,Ti)O_3$ thin films. Appl. Phys. Lett. *112*, 152905.

Tian, B., Liu, L., Yan, M., Wang, J., Zhao, Q., Zhong, N., Xiang, P., Sun, L., Peng, H., Shen, H., et al. (2019). A robust artificial synapse based on organic ferroelectric polymer. Adv. Electron. Mater. *5*, 1800600.

Tuma, T., Pantazi, A., Gallo, M.L., Sebastian, A., and Eleftheriou, E. (2016). Stochastic phase-change neurons. Nat. Nanotechnol. *11*, 693–699.

Wang, M., Cai, S., Pan, C., Wang, C., Lian, X., Zhuo, Y., Xu, K., Cao, T., Pan, X., Wang, B., et al. (2018). Robust memristors based on layered two-dimensional materials. Nat. Electron. *1*, 130–136.

Wen, Z., Wu, D., and Li, A. (2014). Memristive behaviors in $Pt/BaTiO_3/Nb:SrTiO_3$ ferroelectric tunnel junctions. Appl. Phys. Lett. *105*, 052910.

Wurfel, P., Batra, I.P., and Jacobs, J.T. (1973). Polarization instability in thin ferroelectric films. Phys. Rev. Lett. *30*, 1218.

Xing, J., Guo, E.-J., Dong, J., Hao, H., Zheng, Z., and Zhao, C. (2015). High-sensitive switchable photodetector based on $BiFeO_3$ film with in-plane polarization. Appl. Phys. Lett. *106*, 033504.

Yan, X., Zhao, J., Liu, S., Zhou, Z., Liu, Q., Chen, J., and Liu, X.Y. (2018). Memristor with Ag-Cluster-Doped TiO_2 films as artificial synapse for neuroinspired computing. Adv. Funct. Mater. *28*, 1705320.

Yang, C., Shang, D., Liu, N., Fuller, E.J., Agrawal, S., Talin, A.A., Li, Y., Shen, B., and Sun, Y. (2018a). All-solid-state synaptic transistor with ultralow conductance for neuromorphic computing. Adv. Funct. Mater. *28*, 1804170.

Yang, J.T., Ge, C., Du, J.Y., Huang, H.Y., He, M., Wang, C., Lu, H.B., Yang, G.Z., and Jin, K.J. (2018b). Artificial synapses emulated by an electrolyte-gated tungsten-oxide transistor. Adv. Mater. *30*, 1801548.

Yang, S.Y., Seidel, J., Byrnes, S.J., Shafer, P., Yang, C.H., Rossell, M.D., Yu, P., Chu, Y.H., Scott, J.F., Ager, , III, et al.. (2010). Above-bandgap voltages from ferroelectric photovoltaic devices. Nat. Nanotechnol. *5*, 143–147.

Yang, X., Luo, L., Vaswani, C., Zhao, X., Yao, Y., Cheng, D., Liu, Z., Kim, R.H.J., Liu, X., D.-Furdyna, M., et al. (2020). Light control of surface-bulk coupling by terahertz vibrational coherence in a topological insulator. Npj Quant. Mater. *5*, 13.

Yi, H.T., Choi, T., Choi, S.G., Oh, Y.S., and Cheong, S.-W. (2011). Mechanism of the switchable photovoltaic effect in ferroelectric $BiFeO_3$. Adv. Mater. *23*, 3403–3407.

Yuan, Y., Xiao, Z., Yang, B., and Huang, J. (2014). Arising applications of ferroelectric materials in photovoltaic devices. J. Mater. Chem. A. *2*, 6027–6041.

iScience, Volume *23*

Supplemental Information

Highly Controllable and Silicon-Compatible Ferroelectric Photovoltaic Synapses for Neuromorphic Computing

Shengliang Cheng, Zhen Fan, Jingjing Rao, Lanqing Hong, Qicheng Huang, Ruiqiang Tao, Zhipeng Hou, Minghui Qin, Min Zeng, Xubing Lu, Guofu Zhou, Guoliang Yuan, Xingsen Gao, and Jun-Ming Liu

Supplemental Information

Highly-controllable and silicon-compatible ferroelectric photovoltaic synapses for neuromorphic computing

Shengliang Cheng[1,2], Zhen Fan[1,2,7*], Jingjing Rao[1], Lanqing Hong[3], Qicheng Huang[1], Ruiqiang Tao[1], Zhipeng Hou[1], Minghui Qin[1], Min Zeng[1], Xubing Lu[1], Guofu Zhou[2,4], Guoliang Yuan[5], Xingsen Gao[1] and Jun-Ming Liu[1,6]

[1]Institute for Advanced Materials, South China Academy of Advanced Optoelectronics, South China Normal University, Guangzhou 510006, China
[2]Guangdong Provincial Key Laboratory of Optical Information Materials and Technology, South China Academy of Advanced Optoelectronics, South China Normal University, Guangzhou 510006, China
[3]Department of Industrial Systems Engineering and Management, National University of Singapore, Singapore 117576, Singapore
[4]National Center for International Research on Green Optoelectronics, South China Normal University, Guangzhou 510006, China
[5]School of Materials Science and Engineering, Nanjing University of Science and Technology, Nanjing 210094, China
[6]Laboratory of Solid State Microstructures and Innovation Center of Advanced Microstructures, Nanjing University, Nanjing 210093, China
[7]lead contact
*Corresponding author. Email address: fanzhen@m.scnu.edu.cn

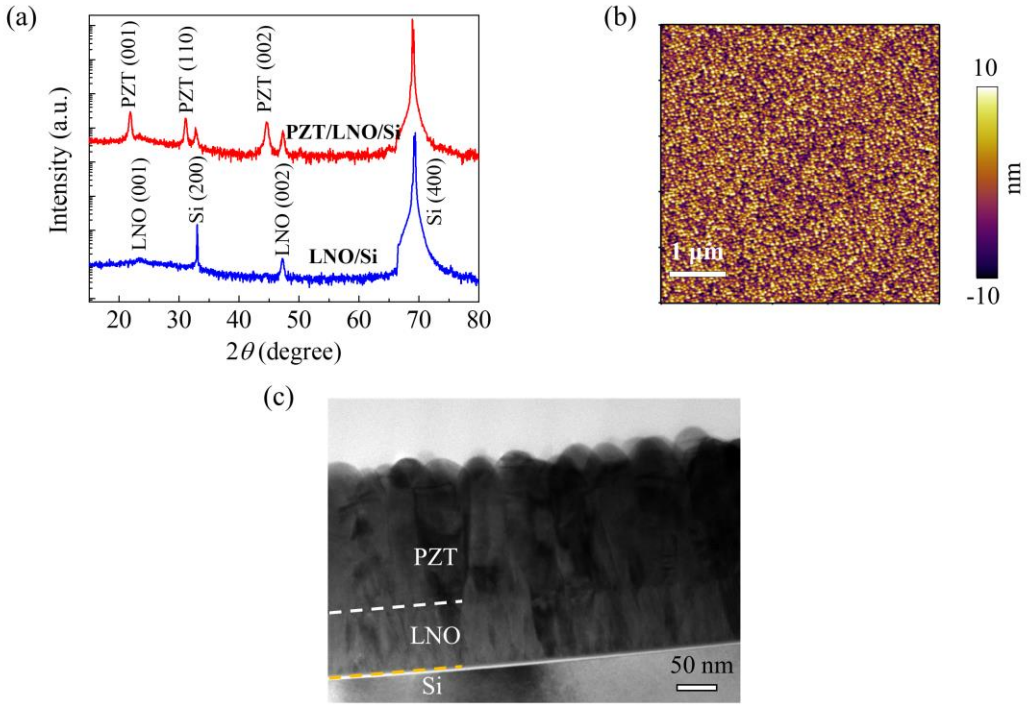

Figure S1. Structural and morphological characterizations of the PZT/LNO/Si film (related to Figure 1). (a) XRD θ-2θ diffraction patterns of a PZT/LNO/Si film and a LNO/Si film (control sample). (b) AFM topography image and (c) cross-sectional TEM image of the PZT/LNO/Si film.

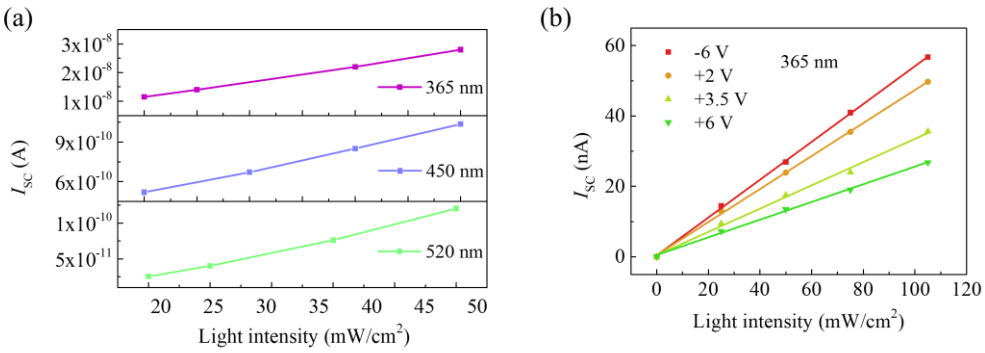

Figure S2. Effects of light wavelength and intensity on photocurrent (related to Figure 1). Photocurrent versus light intensity (a) at different light wavelengths in the P_{up} state and (b) in different polarization states under the illumination of the 365 nm UV light. In b, the polarization states were set by applying -6 V, +2 V, +3.5 V, and +6 V pulses sequentially.

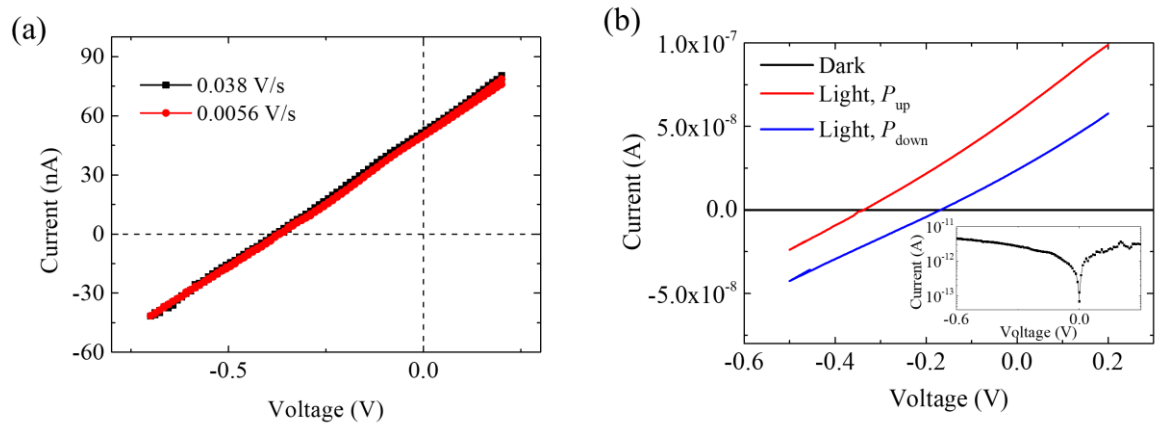

Figure S3. Demonstration of steady photocurrent and comparison between photocurrent and dark current (related to Figure 1). (a) Illuminated *I-V* characteristics measured in the P_{up} state with different voltage sweeping speeds. (b) Comparison between the illuminated and dark *I-V* characteristics. Only the dark *I-V* characteristics the P_{up} state are shown, because the difference between the P_{up} and P_{down} state is small (see Figure S10).

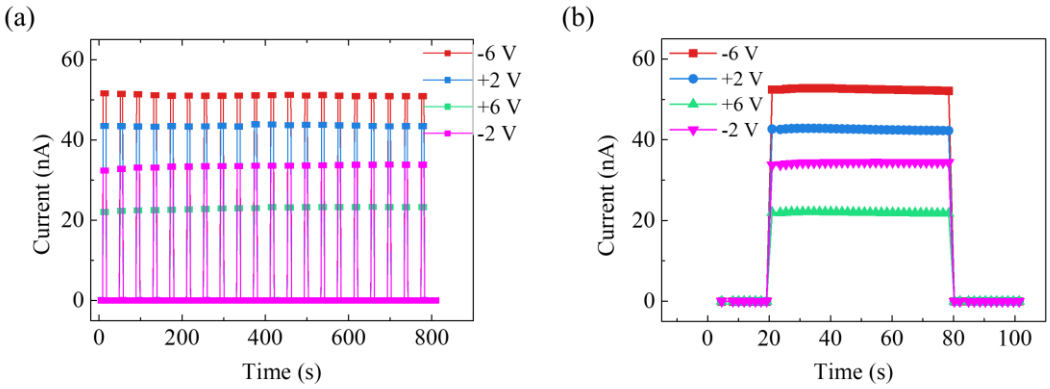

Figure S4. Stability of photovoltaic response (related to Figure 1). (a) Multi-cycle and (b) one-cycle time-dependent photocurrents (read at 0 V) of the Pt/PZT/LNO FePV device measured sequentially after applying -6 V, +2 V, +6 V and -2 V pulses to set different polarization states. In a, the light is switched ON and OFF alternately with 6 and 30 seconds for the ON and OFF periods, respectively. In b, the light is switched ON for an elongated time of ~60 seconds.

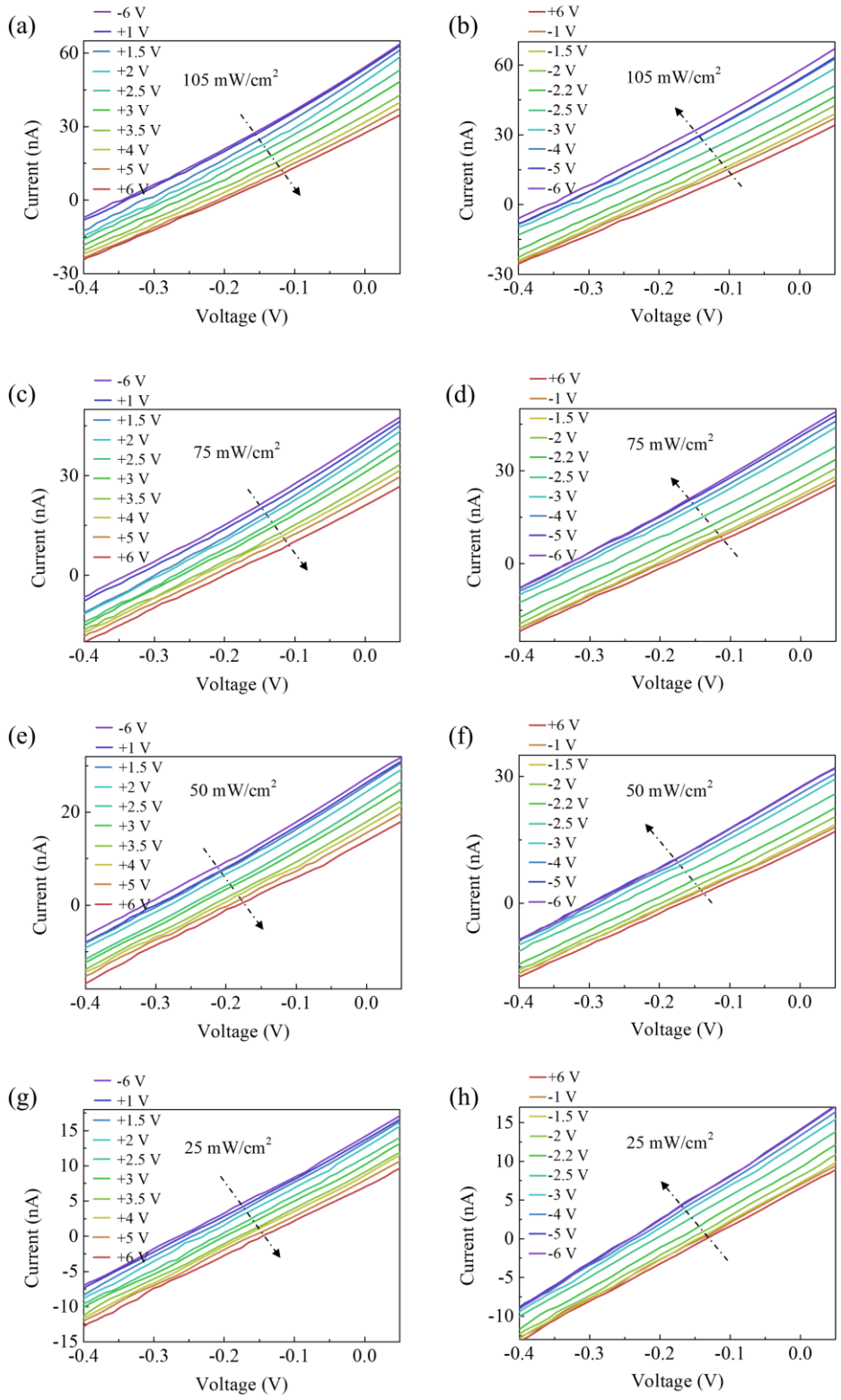

Figure S5. Effect of light intensity on illuminated *I-V* curves (related to Figure 1). Illuminated *I-V* characteristics measured after applying (a,c,e,g) positive pulses from +1 V to +6 V (starting from the initial -6 V pulse-written state) and (b,d,f,h) negative pulses from -1 V

to -6 V (starting from the initial +6 V pulse-written state) at the light intensities of (a,b) 105, (c,d) 75, (e,f) 50, and (g,h) 25 mW/cm^2. Note that the device used here is different from that used for measuring Figure 1 (main text); therefore, the two sets of illuminated *I*-*V* curves at 105 mW/cm^2 shown here and in Figure 1 are not exactly the same.

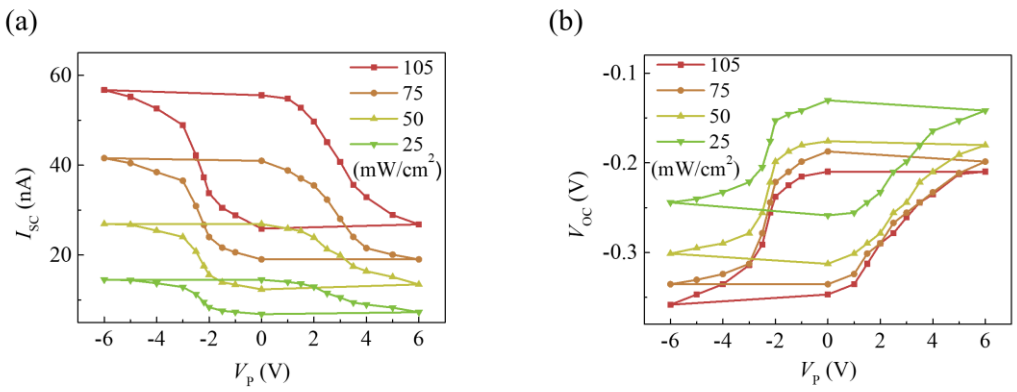

Figure S6. Effect of light intensity on the hysteretic evolutions of I_{SC} and V_{OC} (related to Figure 1). Evolutions of (a) I_{SC} and (b) V_{OC} as a function of pulse amplitude (V_p) at different light intensities. Note that the device used here is different from that used for measuring Figure 1 (main text); therefore, the two sets of the I_{SC} and V_{OC} values at 105 mW/cm^2 shown here and in Figure 1 are not exactly the same.

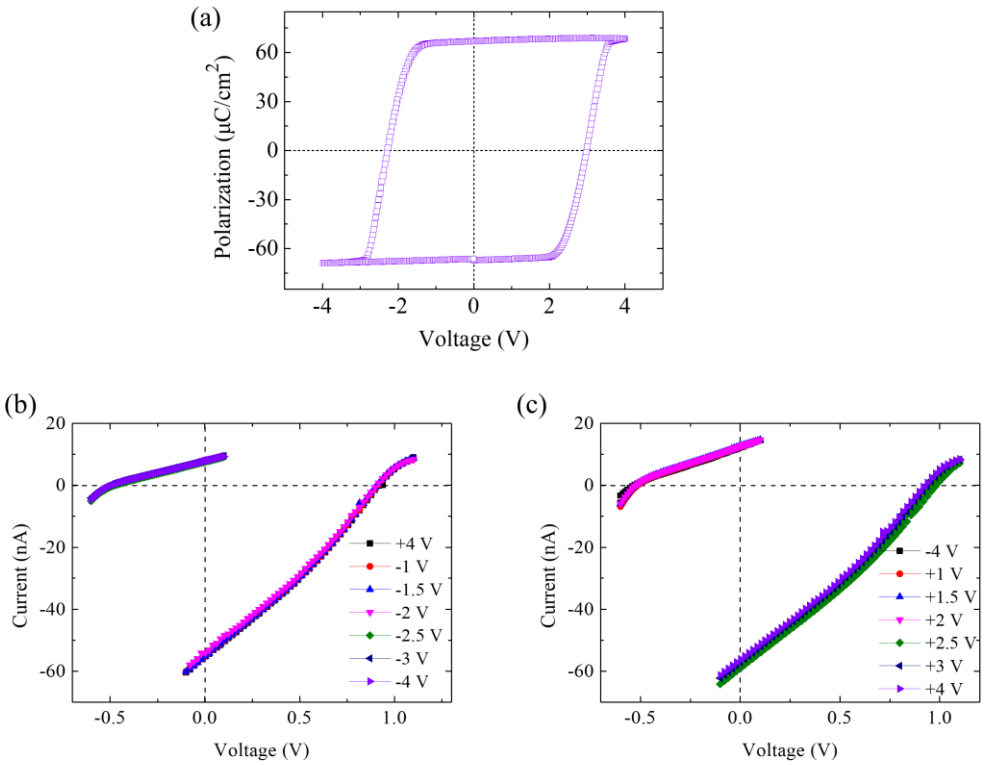

Figure S7. *P-V* hysteresis loop and two bistable photoresponsive states in the epitaxial PZT film (related to Figure 1). (a) Typical *P-V* hysteresis loop of an epitaxial PZT film sandwiched between Pt and $SrRuO_3$ electrodes grown on a $SrTiO_3$ substrate. Illuminated *I-V* characteristics measured after applying (b) negative pulses from -1 V to -4 V (starting from the initial +4 V pulse-written state) and (c) positive pulses from +1 V to +4 V (starting from the initial -4 V pulse-written state).

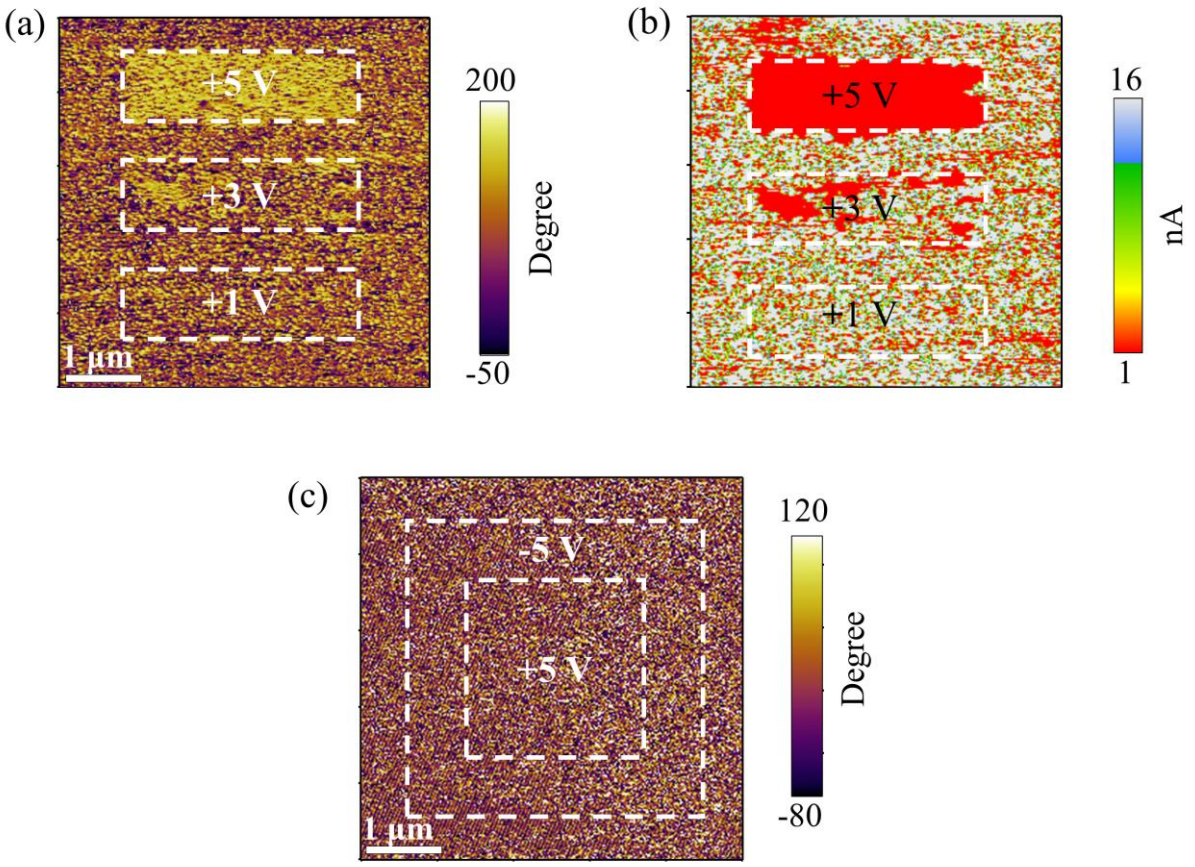

Figure S8. Microscopic observations of concurrent changes in domain configuration and photocurrent (related to Figure 2). (a) PFM phase image and (b) current map under illumination measured after writing three rectangular regions (3 × 1 μm^2) with tip biases of +5 V, +3 V, and +1 V. Note that the measurements in a and b were conducted on the Pt electrode-capped PZT film. (c) PFM phase image taken from a Pt electrode-capped SiO_2/n^{++}-Si control sample.

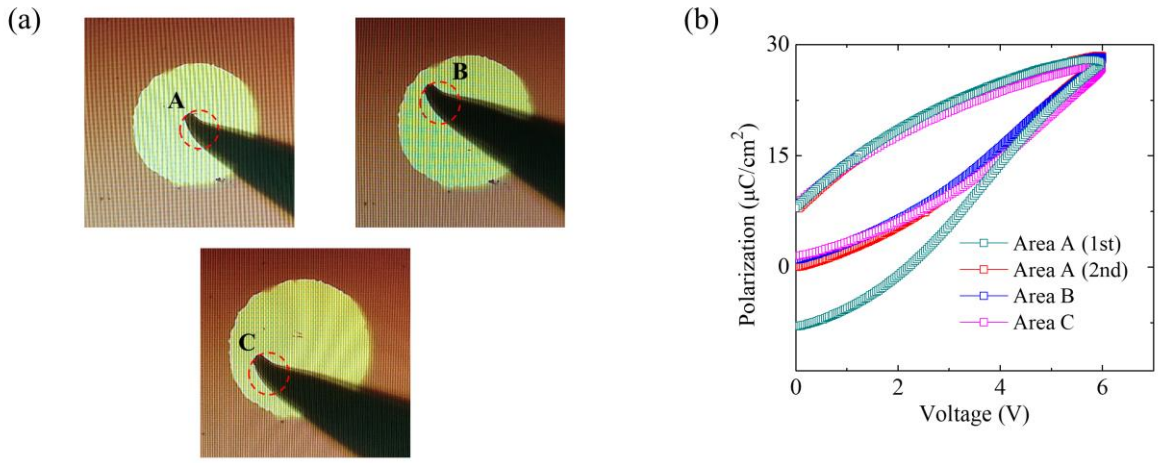

Figure S9. Polarization switching behavior with the tungsten tip-electrode contact (related to Figure 1 and Figure 2). (a) Photographs of the tungsten tip located in the different regions of the Pt electrode. (b) Monopolar *P*-*V* loops measured in the regions marked in a.

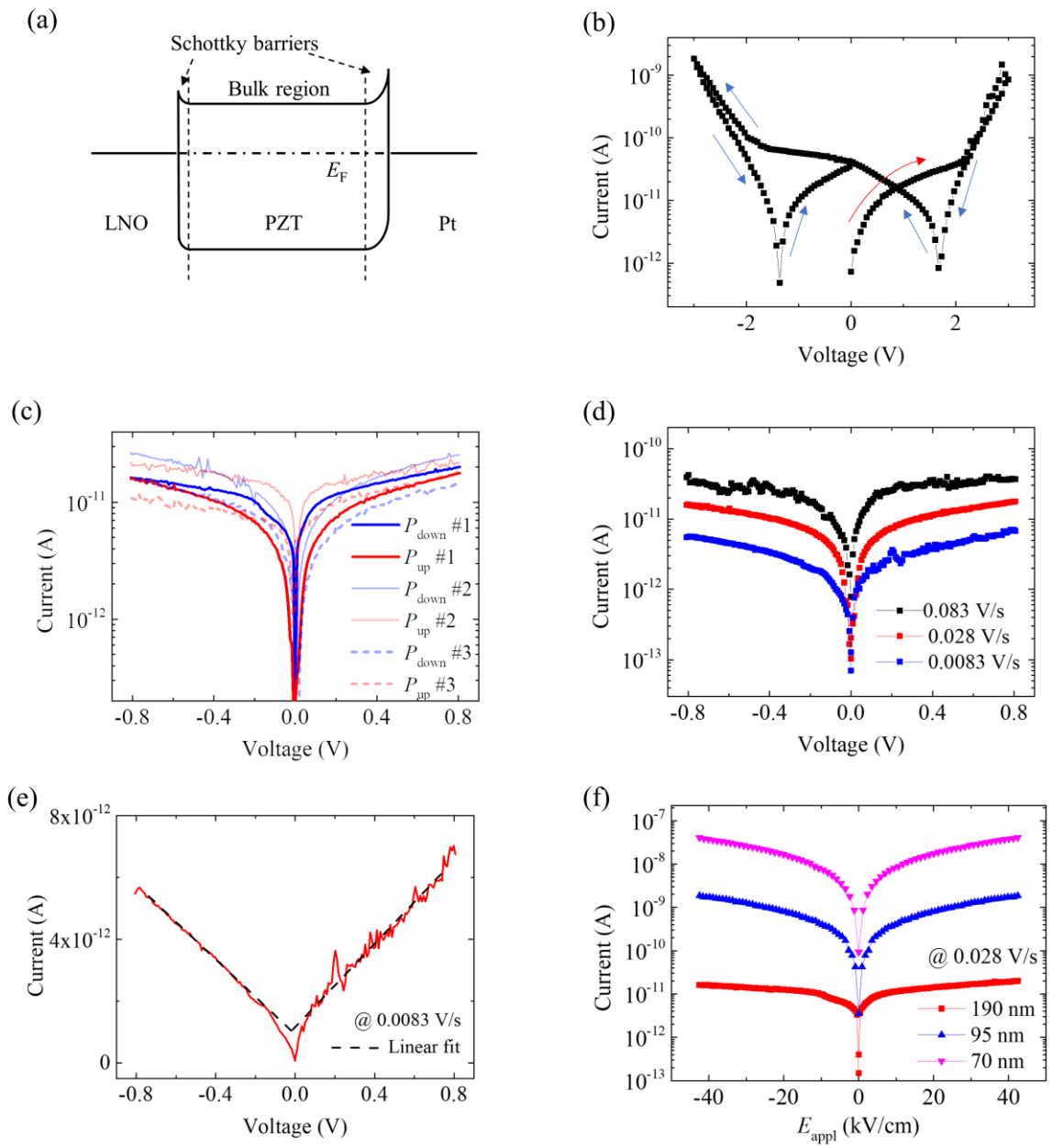

Figure S10. Conduction and photovoltaic mechanisms in the FePV device (related to Figure 1). (a) Schematic energy band diagram of the Pt/PZT/LNO device. (b) Dark *I-V* characteristics measured in the voltage range of +3 V to -3 V at a voltage sweeping rate of 0.06 V/s. The voltage sweeping sequence is indicated by the arrows, and the red arrow indicates the first step. (c) Dark *I-V* characteristics measured in the P_{up} and P_{down} states (set by -6 V and +6 V pulses, respectively) for different cycles. (d) Dark *I-V* characteristics measured in the P_{up}

state at different voltage sweeping rates. (e) Dark *I-V* characteristics plotted in linear scale. (f) Thickness-dependent dark *I-V* characteristics.

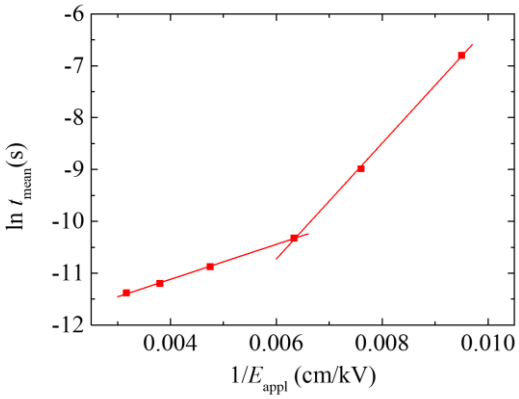

Figure S11. Analysis of domain dynamics based on the Merz's law (related to Figure 2). Relationship between mean switching time (t_{mean}) and applied electric field (E_{appl}) plotted as ln(t_{mean}) versus $1/E_{appl}$.

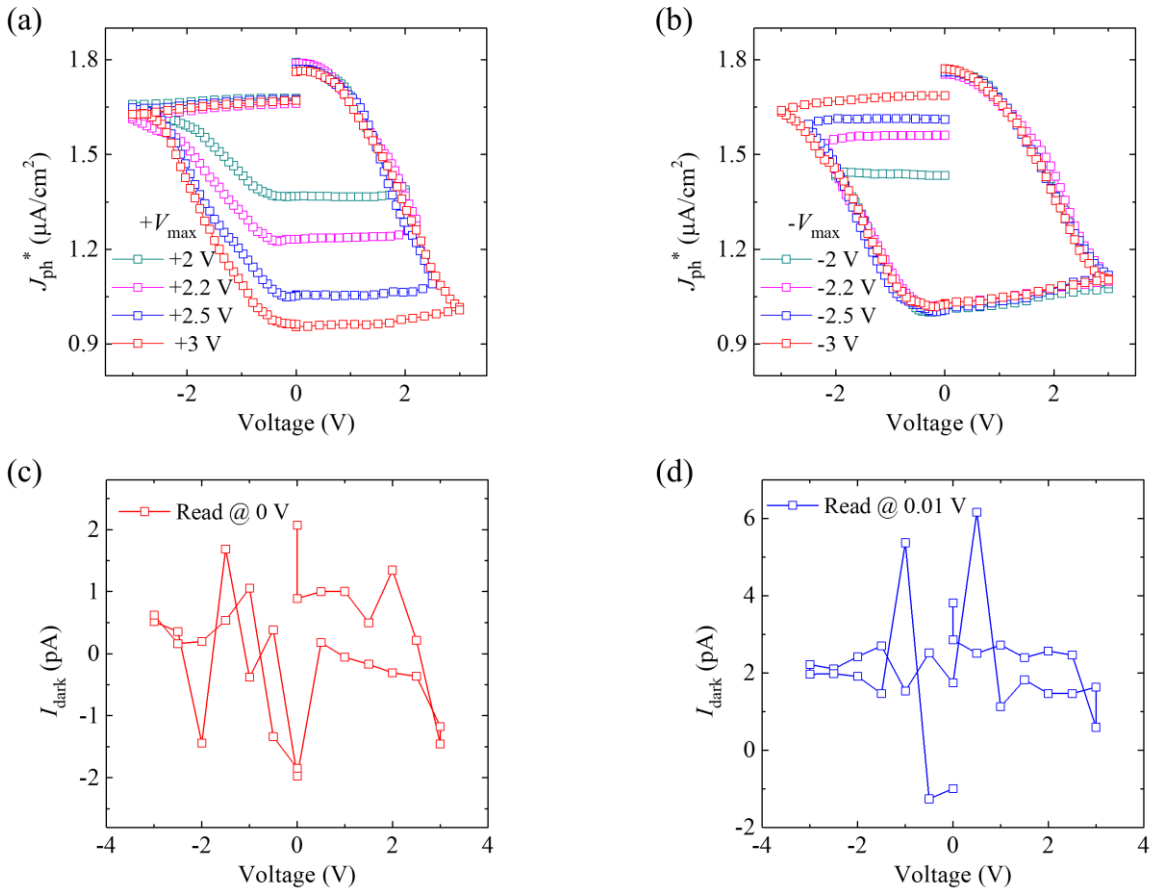

Figure S12. Comparison between photocurrent and dark current in terms of hysteretic behavior (related to Figure 3). J_{ph}^* hysteresis loops obtained with varying (a) $+V_{max}$ and (b) $-V_{max}$ of the triangular pulse trains at the light intensity of 25 mW/cm^2. Dark currents (I_{dark}) read at (c) 0 V and (d) 0.01 V as a function of write pulse amplitude.

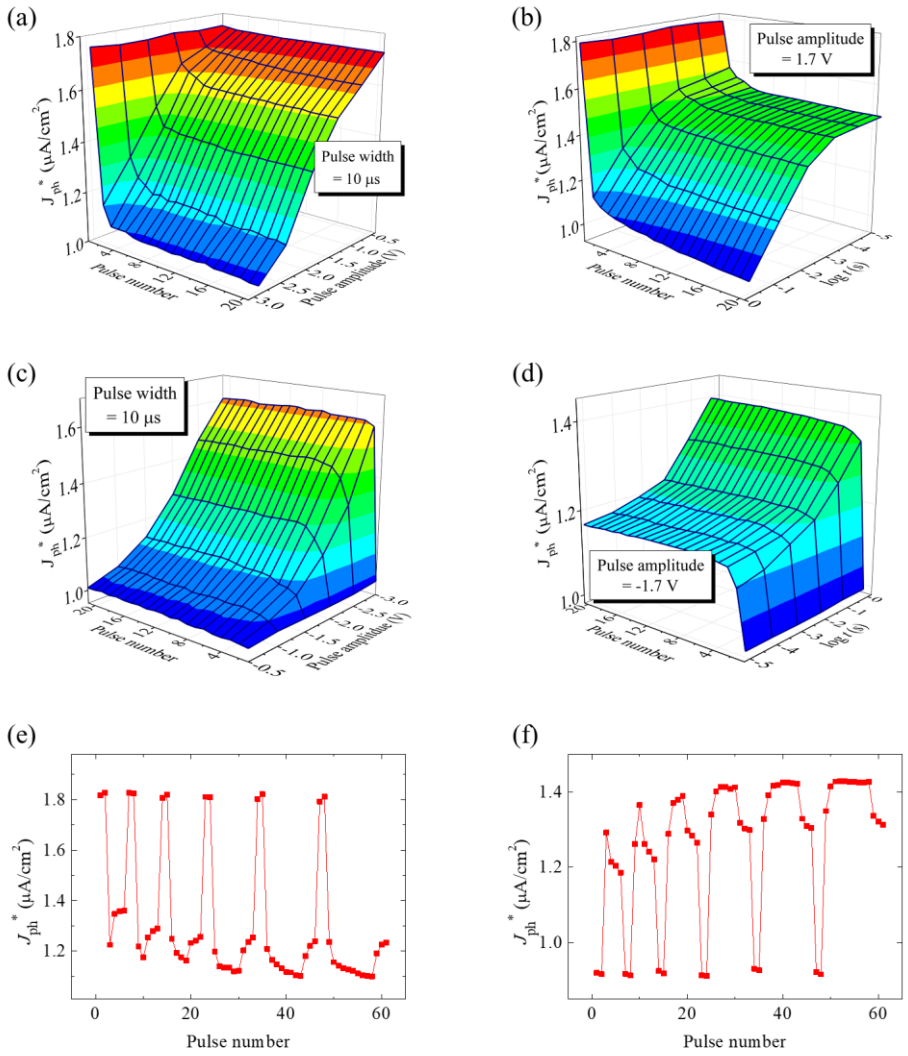

Figure S13. Continuously tunable photovoltaic response measured at the light intensity of 25 mW/cm^2 (related to Figure 3). Evolutions of J_{ph}^* measured using repeated pulses with (a,c) varying pulse number and pulse amplitude while fixing the pulse width, and (b,d) varying pulse number and pulse width while fixing the pulse amplitude. (e) Evolution of J_{ph}^* measured using the negative-positive-negative pulse train where the number of positive pulses (+2.2 V) between two negative pulse groups is varied. (f) Evolution of J_{ph}^* measured using the positive-negative-positive pulse train where the number of negative pulses (-2.2 V) between two positive pulse groups is varied. All the J_{ph}^* data were measured at the light intensity of 25 mW/cm^2.

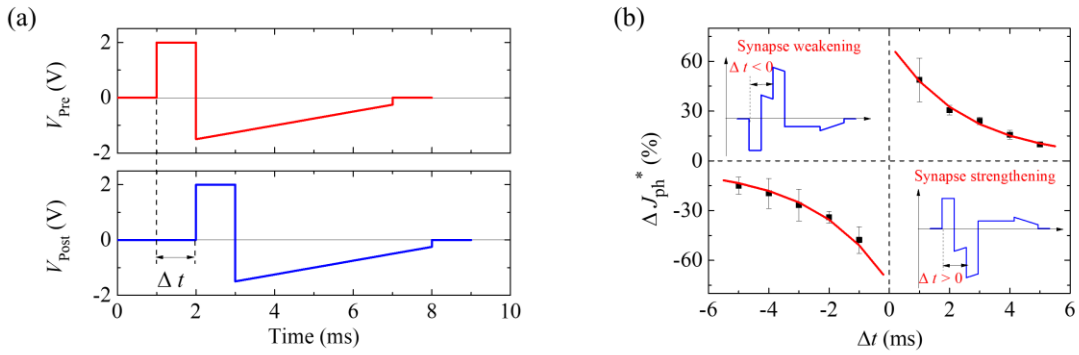

Figure S14. STDP behavior (related to Figure 4). (a) Voltage waveforms of pre- and post-synaptic spikes. (b) STDP characteristics of the Pt/PZT/LNO FePV synapse. Inset in b shows the superposed waveforms of the pre- and post-synaptic spikes.

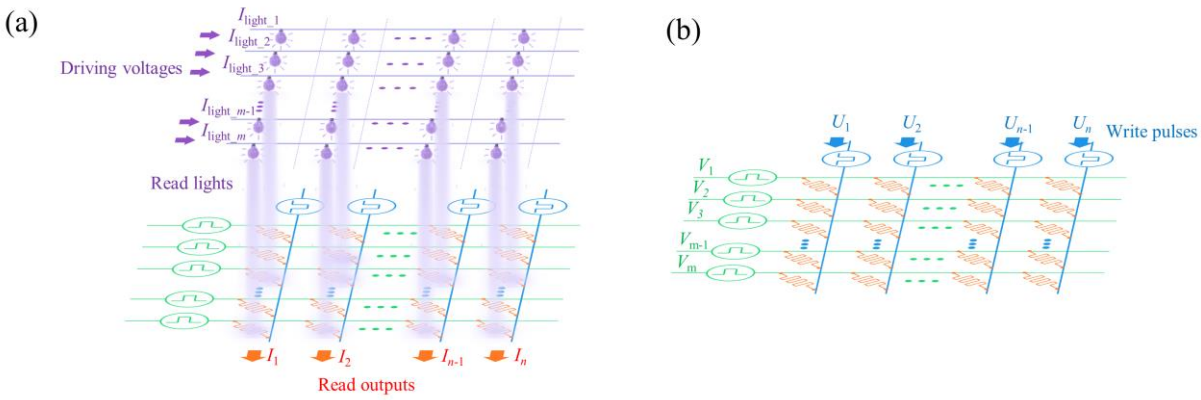

Figure S15. FePV synapse-based neural network (related to Figure 4). Schematics illustrating the (a) read and (b) write operations of the FePV synapse-based neural network.

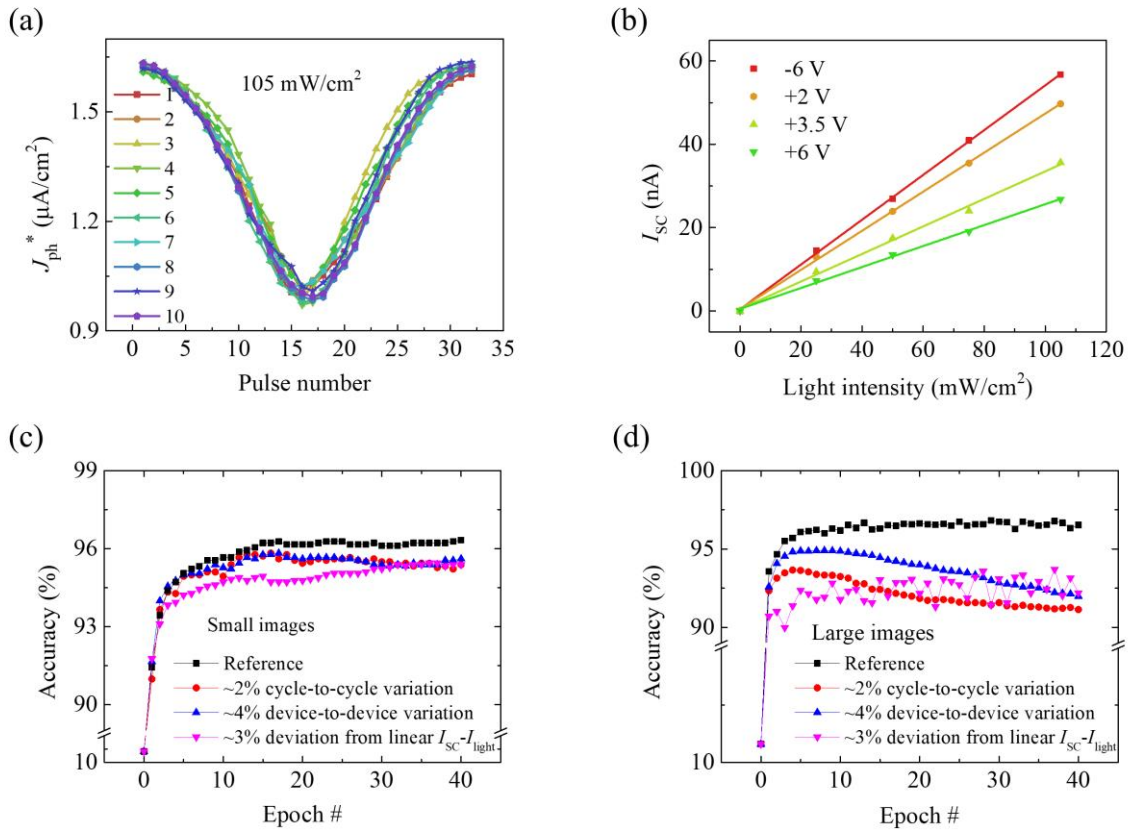

Figure S16. Effects of non-ideal factors on the simulated accuracy (related to Figure 4). (a) One-cycle LTP/LTD characteristics of 10 different FePV devices (applied pulses are the same as those in Figure 4a in the main text). (b) Photocurrent versus light intensity in different polarization states under the illumination of the 365 nm UV light. Effects of cycle-to-cycle variation, device-to-device variation, and realistic dependence of photocurrent on light intensity on the accuracies for recognizing (c) small and (d) large images. In c and d, "Reference" denotes the case where the cycle-to-cycle and device-to-device variations are zero and the dependence of photocurrent on light intensity is ideally linear.

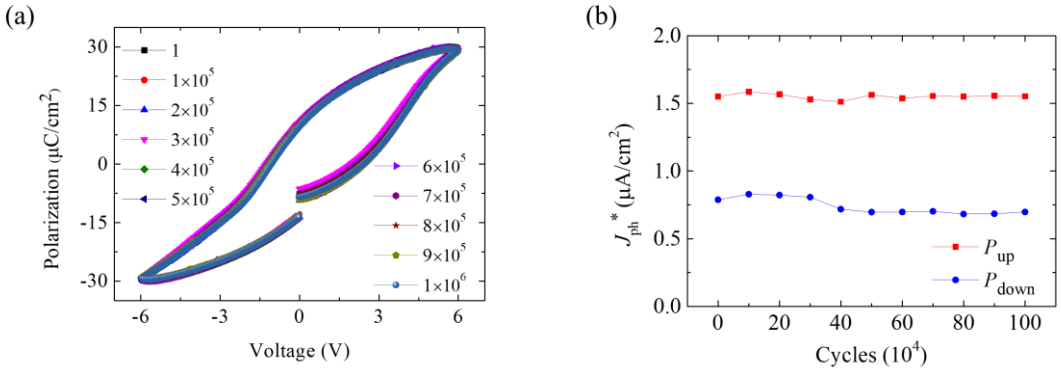

Figure S17. Endurance characteristics (related to Figure 5). Evolutions of (a) *P*-*V* hysteresis loops and (b) J_{ph}^{*} in the P_{up} and P_{down} states with increasing the number of switching cycles.

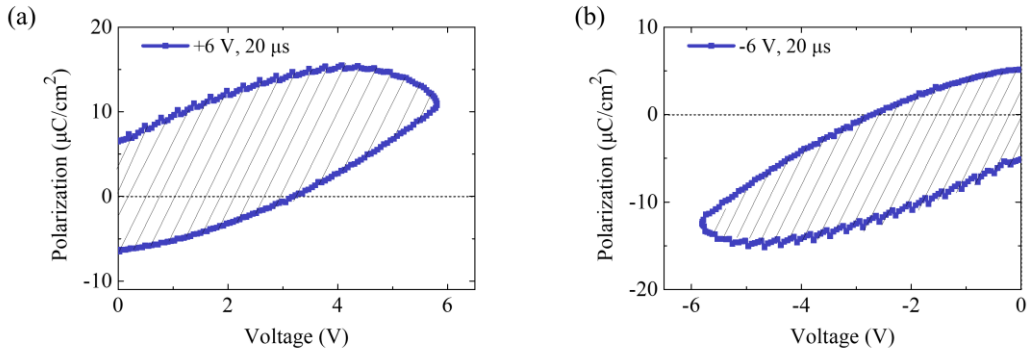

Figure S18. *P-V* loops for the energy consumption estimation (related to Figure 5). Typical monopolar *P-V* hysteresis loops measured with (a) +6 V/20 μs and (b) -6V/20 μs pulses.

Table S1. Comparison of performances of neural networks based on different synaptic devices (related to Figure 4).

Device structure	Accuracy (%)	Dataset	Operating principle
Ag/BTO/NSTO (Ma et al., 2020)	~90	MNIST	Ferroelectric domain switching
Pt/BTO/SNTO (Li et al., 2019)	96.5 96.4	ORHD[a] MNIST	Ferroelectric domain switching
α -MoO_3 transistor (Yang et al., 2018)	94.1 87.3	ORHD MNIST	Li ions intercalation
$Si_{0.9}/Ge_{0.1}$ (Choi et al., 2018)	95.1	MNIST	Ag ion filament
PEI/PEDOT:PSS (van de Burgt et al., 2017)	93.0 97.0	SFC[b] MNIST	Proton doping
BM-SFO transistor (Ge et al., 2019)	95.2 92.7	ORHD MNIST	Phase transformation
VO_2 transistor (Ge et al., 2020)	94.0 91.0	ORHD MNIST	Phase transformation
Li-ion transistor (Fuller et al., 2017)	97.5 93.0	SFC MNIST	intercalation of Li-ion dopants
Pt/PZT/LNO (this work)	95.4 93.7	ORHD MNIST	Ferroelectric domain switching

[a)]ORHD: Optical Recognition of Handwritten Digits

[b)]SFC: Sandia file classification

Transparent Methods

1. Device Fabrication

Stoichiometric $LaNiO_3$ (LNO) and nonstoichiometric $Pb(Zr_{0.2}Ti_{0.8})O_3$ (PZT) with 15% Pb excess ceramic targets with a purity of 99.99% were bought from the Hefei Kejing Materials Technology Co., Ltd, which were used for the pulsed laser deposition (PLD) of polycrystalline LNO and PZT thin films on silicon (100) substrates, respectively. Our PLD system mainly consisted of a KrF (λ = 248 nm) excimer laser source (Coherent COMPexPro 205) and a customized chamber (TSST HE-B01 and TE-R08). The ~80 nm thick LNO bottom electrode layers were first deposited on the silicon substrates at 660 °C under an oxygen pressure of 15 Pa. Subsequently, the ~190 nm thick PZT layers were grown on top of the LNO layers at a lower temperature of 600 °C with the same oxygen pressure. For the LNO and PZT depositions, different laser energy densities of ~1.2 and ~0.9 J/cm^2 were used, respectively, while the laser pulse frequency was kept at the same 5 Hz. In addition, epitaxial PZT films, as control samples, were deposited on the $SrRuO_3$ (SRO)-buffered $SrTiO_3$ (001) substrates. The growth temperatures of the epitaxial PZT and SRO films were 615 and 680 °C, respectively, while the same oxygen pressure of 15 Pa was used for both films. The Pt top electrodes of ~200 μm in diameter and ~10 nm in thickness were *ex situ* deposited on the films by PLD through a shadow mask at room temperature and under vacuum.

Note that all the film depositions were conducted in our lab, while previous studies (Schatz et al., 2017; Yu et al., 2007; Kim et al., 2000) were referred to for optimizing the deposition parameters of the polycrystalline PZT films on silicon substrates.

2. Characterizations

The phases and crystal structures of the films were examined by X-ray diffraction (XRD) (X'Pert PRO, PANalytical). The microstructures of the films were characterized using a Tecnai

G2-F20 transmission electron microscopy (TEM) system operated at 200 kV. The film morphology, domain switching, and current mapping were studied by atomic force microscopy (AFM), piezoresponse force microscopy (PFM), and conductive AFM (C-AFM), respectively. The AFM, PFM, and C-AFM measurements were performed on a commercial atomic force microscope (Cypher, Asylum Research) with Pt-coated silicon tips (EFM Arrow, Nanoworld).

3. Electrical Measurements

The polarization-voltage (*P*-*V*) hysteresis loop, positive-up negative-down (PUND), and endurance tests were conducted with a ferroelectric workstation (Precision Multiferroic, Radiant). The current-voltage (*I*-*V*) characteristics were measured using a SourceMeter (6430, Keithley) with an automatic voltage sweeping program. Both the ferroelectric workstation and SourceMeter can generate electrical pulses with various amplitudes and widths (ranging from 10 μs to 1 s). For the photovoltaic measurements, an ultraviolet light-emitting diode (LED) with tunable light intensities and a wavelength of 365 nm was mainly used as the light source. Unless otherwise specified, the electrical pulse interval was fixed at 1 s, and the light intensity was fixed at 105 mW/cm^2. When measuring the illuminated *I*-*V* characteristics, the light was switched on ~10 seconds before the measurement to exclude the contribution from the transient photocurrent response, and a sufficiently low voltage sweeping speed (~0.038 V/s) was used to record the steady current (see Figure S3a).

4. Neural Network Simulations

The neural network simulations were conducted using a CrossSim simulator (van de Burgt et al., 2017; Fuller et al., 2017) based on the back-propagation algorithm. The simulator used a three-layer (one hidden layer) neural network, and each synaptic weight matrix between two neuron layers was modeled as a crossbar. The crossbar performed two matrix operations: vector-matrix multiply and parallel rank one outer product update. The numerical weights in a crossbar were mapped directly onto the experimental J_{ph}^{*} values measured in the

potentiation/depression cycling test (see Figure 4a in the main text), and thus the numbers of weight levels were 16 for both the potentiation and depression processes. The number of neurons and synapses used in the image recognition simulations were dependent on the image datasets. For small images (8 × 8 pixels), 64, 36, and 10 neurons were used in the input, hidden, and output layers, respectively. The numbers of synapses in the two crossbars were therefore 2304 (64 × 36) and 360 (36 × 10), respectively. For large images (28 × 28 pixels), a network size of 784 × 300 × 10 was used. When training a neural network, 3823 and 60000 examples were used for small and large images, respectively. Afterwards, the accuracy of the neural network was tested with 1797 (10000) examples for small (large) images. The learning rates for the simulations of small and large image recognitions were optimized to be 0.15 and 0.025, respectively.

5. Data Analysis for Figure S1

Figure S1a shows the XRD θ-2θ diffraction patterns of a PZT/LNO/Si bilayer film and a LNO/Si film, with the latter as the control sample. The (001) and (110) peaks from PZT are clearly identified, indicating that polycrystalline PZT with a perovskite phase is formed. There are no peaks from impurity phases, demonstrating the phase purity of the PZT film. Figure S1b displays that the polycrystalline PZT film exhibits a granular surface, with a relatively small roughness of ~4 nm. The cross-sectional TEM image, as shown in Figure S1c, demonstrates that the PZT film is tightly adhered to the LNO layer with a sharp interface. Additionally, the PZT film exhibits columnar grains, which are ~190 nm in height and ~50 nm in diameter.

6. Data Analysis for Figure S2

Figure S2a shows that at the same light intensity the 365 nm UV light produces the highest photocurrent, which is consistent with the fact that PZT has a relatively wide bandgap of ~3.6 eV (Tan et al., 2019). In addition, as shown in Figure S2b, in all the different polarization states the photocurrent scales almost linearly with the light intensity. As seen from the above results,

the 365 nm UV light with the intensity of 105 mW/cm^2 is a suitable illumination condition. Therefore, this illumination condition was mainly used in the main text.

7. Data Analysis for Figure S3

As shown in Figure S3a, although the voltage sweeping speed decreases from ~0.038 V/s to ~0.0056 V/s, the photovoltaic *I-V* curve remains almost unchanged, demonstrating that the current values measured at ~0.038 V/s are already steady ones. In addition, the light was switched ON ~10 seconds before the *I-V* measurement to exclude the contribution from the transient photocurrent response. Figure S3b shows that the photocurrent is orders of magnitude larger than the dark current at low voltage. In addition, measuring the photocurrent at zero voltage has technically eliminated the contribution from the dark current.

8. Data Analysis for Figure S4

Applications of -6 V and +6 V write pulses (pulse width: 1 ms) result in the fully upward and downward polarization states, respectively. On the other hand, applications of +2 V pulse (after the -6 V pulse) and -2 V pulse (after the 6 V pulse) (pulse width: 10 μs) result in two intermediate polarization states. Figure S4 show that the photocurrents measured in all these states are quite stable and reproducible, indicating the nonvolatility of the photoresponsive states. In Figure S4b, no spike is observed right after the light is switched ON, probably because the photocurrent response time in our polycrystalline PZT film is sufficiently short (less than ~1.8 seconds, i.e., the time resolution used in the photocurrent-time measurement). This allows us to measure the steady current when performing the photovoltaic *I-V* measurement.

9. Data Analysis for Figure S5 and Figure S6

Figure S5 shows that the successive shift of the illuminated *I-V* curve with applied write pulse occurs at the different light intensities. In addition, both I_{SC} and V_{OC} show hysteretic evolutions with varying pulse amplitude at different light intensities (see Figure S6). The I_{SC}

and V_{OC} values in the same polarization state increase as the light intensity increases, indicating that the I_{SC} and V_{OC} are light-induced. The above results well demonstrate the phenomenon of polarization-modulated switchable photovoltaic response.

10. Data Analysis for Figure S7

Figure S7a shows the square *P*-*V* hysteresis loop observed in the epitaxial PZT film, indicating that two typical bistable polarization states exist and the switching between these two states is abrupt. Consequently, there are two bistable photoresponsive states and the switching between them is also observed to be abrupt, as shown in Figure S7b,c.

11. Data Analysis for Figure S8

Three rectangular regions (3×1 μm^2) were written with tip biases of +5 V, +3 V and +1 V, respectively, and then PFM and C-AFM images were measured. The C-AFM measurement was conducted with the sample bias but zero sample bias was indeed applied for measuring the photocurrent. The sign of the measured photocurrent was reversed because the current flowing from top to bottom was defined to be positive.

Figure S8a displays that almost all domains in the +5 V-written region and partial domains in the +3 V-written region are switched downward, while the domains in the +1 V-written region remain almost unchanged. The different degrees of domain switching lead to different changes in photocurrent. As shown in Figure S8b, the photocurrents in the whole +5 V-written region are decreased significantly, while in the +3 V-written region only the photocurrents in the parts where domains are switched downward are decreased. However, the photocurrents in the +1 V-written region are similar to those in the unwritten region. The combined PFM and C-AFM results therefore confirm that the photovoltaic response is modulated by the polarization.

Note that the Pt top electrode was used to enhance the magnitude of photocurrent; otherwise, the photocurrent can hardly be detected using the AFM tip-film contact. The Pt electrode may decrease the interfacial barrier height or increase the contact area, thereby enhancing the

magnitude of photocurrent. However, the local switching of domains is observed with the Pt electrode. To understand the origin, a similar electrical writing was performed on a Pt electrode-capped SiO_2/n^{++}-Si control sample. The resultant PFM phase image shows no changes in the written areas (Figure S8c), thus excluding the surface effect-induced artifacts. We therefore think that the Pt electrode may not be an ideal conductor, because it was thin (~10 nm) and composed of nanosized grains. Therefore, electrically writing on the Pt electrode-capped PZT film using the AFM tip induces the domain switching and photocurrent change only in a local area (see Figure S8a,b). This local switching behavior with a non-ideal top electrode was reported previously (Li et al., 2017).

Indeed, for a non-ideal electrode, the tip-generated field drops as a nonlinear function of distance from the tip-electrode contact along the in-plane direction (Li et al., 2017). This means that when a voltage V is applied via the tip, the potential V_1 in the tip-electrode contact area (A_0) is larger than the potential V_2 in the area outside A_0 (note: we use this qualitative description because the exact function of the potential distribution is unknown). This non-uniform potential distribution may cause non-uniform domain switching within the electrode area. Nevertheless, when V is sufficiently large, both V_1 and V_2 exceed coercive voltage (V_c) and thus the domains in and outside the area A_0 can be switched. The total area where the domains are switched (A_s) therefore depends on the voltage V and the tip-electrode contact area A_0. For a given V, if A_0 is larger, a larger area is subjected to V_1 and thus more domains can be switched.

The AFM tip has a very small A_0 (tip radius: ~15 nm). Even if $A_s/A_0 = 100$ is assumed, the resultant radius of A_s is ~150 nm, which is still very small. Therefore, using the AFM tip to write on the electrode can cause a local switching. By contrast, the tungsten tip has a much larger A_0 of $\sim 1.5 \times 10^{-5}$ cm^2 (confirmed by checking the scratch left by tungsten tip), about ~5% of the whole electrode area. If V is sufficiently large, it could be possible that A_s becomes the whole electrode area (see the demonstration in Figure S9).

12. Data Analysis for Figure S9

For the tungsten tip-electrode contact, to verify whether A_s can be the whole electrode area under a large voltage, we first located the tungsten tip in Region A, B, and C, and applied -6 V pulses to set the polarization states of all the three regions to P_{up}. Then, the tungsten tip was located in Region A and two +6 V pulse were applied sequentially. The measured monopolar *P*-*V* loops are shown in Figure S9b. The first +6 V pulse switches the polarization to the downward direction and therefore an "S"-shaped loop is present. However, the loop measured by the second +6 V pulse does not exhibits an apparent "S" shape. This is because the polarization is already along the downward direction, and hence this loop is contributed mainly by non-ferroelectric factors, such as leakage current and linear dielectric response. Then, we moved the tungsten tip to Region B and C sequentially, and measured the monopolar *P*-*V* loop in each region by applying a +6 V pulse. The loops measured in both Region B and C are similar to that measured in Region A with the second +6 V pulse, indicating that the domains in Region B and C have already been switched to the downward direction after applying +6 V pulses in Region A. This in turn supports that applying a sufficiently large voltage via the tungsten tip-electrode contact can switch the domains in the whole electrode area.

13. Data Analysis for Figure S10

Generally, there are four FePV mechanisms accounting for the polarization modulation of photovoltaic response: bulk photovoltaic effect, domain wall model, Schottky barrier model, and depolarization field (E_{dp}) model.

The bulk photovoltaic effect often occurs in a single crystal, where the photo-generated charge carriers with asymmetric momentum distribution can exhibit collective motion along a certain direction (Fridkin et al., 2001). However, our PZT film is polycrystalline, the momentum distributions of photo-generated charge carriers may cancel each other out. Therefore, the bulk photovoltaic effect may be neglected in our polycrystalline PZT-based FePV device. In addition,

the domain walls in the polycrystalline PZT film are not aligned in parallel, which rules out the domain wall model as the major photovoltaic mechanism in our FePV device.

To check the applicability of the Schottky barrier model, the energy band alignment of the Pt/PZT/LNO heterostructure is first analyzed. Because Pt and LNO have work functions of ~5.6 eV (Yan et al., 2010) and ~4.5 eV (Yang et al., 2012), respectively, and PZT has an electron affinity of ~3.5 eV (Cagin et al., 2007), two Schottky barriers with much different heights may exist in the Pt/PZT/LNO heterostructure (see Figure S10a). If the conduction is dominated by the Schottky barriers, *I-V* curves with large asymmetry are expected. However, the asymmetry of the observed dark *I-V* curves is rather small (Figure S10b). In addition, Figure S10b and c also reveal that the switchable diode-type resistive switching behavior is absent. In Figure S10b, a small hysteresis is observed when the voltage sweeping direction is reversed and the dark current (I_{dark}) becomes zero at a non-zero voltage, both of which can be correlated with the change of the capacitive current (I_{cap}) due to the reverse of the sign of dV/dt and the change of capacitance [note: $I_{cap} = C^*(dV/dt)$]. In Figure S10c, I_{dark} randomly varies from cycle to cycle and it does not show a variation trend with respect to the polarization state. This can be well explained by the randomness of I_{cap}, which may originate from the random capacitance variation caused by the pulse writing-induced charge injection and redistribution. The contribution from I_{cap} to I_{dark} can be evidenced by measuring the dark *I-V* characteristics at different voltage sweeping rates (i.e., dV/dt). Figure S10d shows that the measured I_{dark} increases with voltage sweeping rate, confirming the contribution from I_{cap} to I_{dark}.

Therefore, the above results rule out the Schottky barrier-dominated conduction mechanism and the ferroelectric memristive effect. They also demonstrate that I_{cap} can significantly contribute to the measured $I_{dark,}$ particularly when the current level is low.

While the polycrystalline PZT film has a thickness of ~190 nm, a large bulk region exists (Figure S10a) and may greatly influence the conduction and associated FePV effect. Indeed, the dark *I-V* curves can be well fitted to the Ohmic model (see Figure S10e), suggesting that

the conduction mechanism (in the voltage region of -0.8 V to 0.8 V) is bulk-limited (note: to minimize the involvement of I_{cap}, the dark *I-V* curve measured at a very slow rate of 0.0083 V/s was used for fitting). Moreover, I_{dark} decreases with increasing film thickness (see Figure S10f), agreeing well with bulk-limited conduction behavior. For our polycrystalline PZT film, therefore, the conduction mechanism is bulk-limited and consequently a bulk mechanism should also be responsible for the FePV effect.

The only left bulk mechanism for the FePV effect is the E_{dp} model. In this model, a switchable E_{dp} and an unswitchable internal bias field (E_{int}) may be considered as the driving forces for the photovoltaic effect. E_{dp} arises from the incomplete screening of polarization, while E_{int} may be formed due to stress gradients (Zhou et al., 2005), asymmetric electrodes (Lee et al., 1998), and non-uniformly distributed space charges (Tagantsev et al., 2004). How E_{dp} and E_{int} modulate the photovoltaic response is explained in the main text.

14. Data Analysis for Figure S11

The relationship between t_{mean} and pulse amplitude can be described using the Merz's law:

$$t_{mean} \propto \exp\left(\alpha / E_{appl}\right), \tag{S1}$$

where α is the activation field and E_{appl} is the applied electric field (i.e., the pulse amplitude divided by the film thickness). As shown in Figure S11, the $\ln(t_{mean})$-$1/E_{appl}$ curve exhibits two linear regions with different slopes. The α values in the low-E_{appl} and high-E_{appl} regions are ~1100 and ~340 kV/cm, respectively. These α values are consistent with those reported for the PZT films (So et al., 2005; Jo et al., 2007). In addition, the change of α as E_{appl} increases was also observed previously (So et al., 2005), which may be attributed to the different nucleation rates in the low-E_{appl} and high-E_{appl} regions.

15. Data Analysis for Figure S12

Figure S12a,b show the evolutions of J_{ph}^* with the pulse amplitudes measured at the light intensity of 25 mW/cm^2 using the triangular pulse trains. The J_{ph}^* evolutions form the hysteresis loops and multiple intermediate J_{ph}^* levels can be obtained, similar to those measured at the light intensity of 105 mW/cm^2 (Figure 3b,c in the main text).

When no illumination is applied, the dark currents (I_{dark}) read at 0 V are simply noisy signals and no variation trend of I_{dark} is observed as the pulse amplitude varies (Figure S12c). We also conducted the same measurement with the I_{dark} read at 0.01 V. Again, I_{dark} does not show hysteretic evolution with varying pulse amplitude (Figure S12d). This is consistent with the absence of ferroelectric memristive effect in our polycrystalline PZT film (see Figure S10 and related discussion).

In addition, the variations of J_{ph}^* as a function of pulse amplitude, width, and history were measured at the light intensity of 25 mW/cm^2. The results are shown in Figure S13, which are basically similar to those measured at the light intensity of 105 mW/cm^2 (Figure 3d-i in the main text).

16. Data Analysis for Figure S15

In the read operation, no read voltages are applied along the rows (see Figure S15a). Because for our FePV synapses J_{ph}^* exhibits a highly linear dependence on the light intensity (see Figure S2), the pixel values of the input images are thus encoded as the light intensities. Consequently, the output photocurrent along the *j*th column is

$$I_j = \sum_{i=1}^{m} J_{ph\_ij}^* \times \left[I_{light\_i} / (1\ \text{mW/cm}^2) \right] \times A \qquad \text{(S2)}$$

where $I_{light\_i}/(1\ \text{mW/cm}^2)$ is the normalized light intensity applied along the *i*th row and *A* is the device area of a single synapse. Eq. (S2) indicates that a parallel read operation or a vector-matrix multiply is realized with the FePV devices used as the synapses. To represent the negative weights, a bias row and column can be added, which are not drawn here.

In the write operation, the programming pulses (U_j) are applied along the columns corresponding to the selected synapses while the corresponding rows are grounded ($V_i = 0$) (here, i and j are the row and column indices of the selected synapses). The number and amplitude of the programming pulses are calculated based on the desired weight updates obtained from the back-propagation algorithm. In this way, the weights of all the selected synapses can be updated appropriately. For the unselected rows and columns, the half-voltage scheme may be employed to reduce the write disturbance.

17. Data Analysis for Figure S16

First, the accuracies of the neural networks with and without considering the cycle-to-cycle variation were computed. As the cycle-to-cycle variation changes from 0 to the experimental value of ~2%, the accuracy decreases from 96.3% (@ 40th epoch) to 95.8% (@ 16th epoch) for recognizing small images (Figure S16c), while that decreases from 96.8% (@ 29th epoch) to 93.7% (@ 4th epoch) for recognizing large images (Figure S16d). Then, the LTP/LTD characteristics of 10 different devices were measured and are shown in Figure S16a, based on which the device-to-device variation is estimated as ~4%. Figure S16c,d compares the accuracies of the neural networks with and without considering the device-to-device variation. As the device-to-device variation changes from 0 to ~4%, the accuracy decreases from 96.3% (@ 40th epoch) to 95.8% (@ 17th epoch) for recognizing small images (Figure S16c), while that decreases from 96.8% (@ 29th epoch) to 94.9% (@ 8th epoch) for recognizing large images (Figure S16d). Similar degradations of neural network performance with the cycle-to-cycle and device-to-device variations were reported in Ref. (Ma et al., 2020).

We also considered the factor of the realistic dependence of photocurrent (I_{SC}) on light intensity (I_{light}). As shown in Figure S16b, the realistic dependence deviates from the ideal linear dependence, and the deviation is ~3%. This means that $J_{ph}^{*} = I_{SC}/A/[I_{light}/(1\ mW/cm^2)]$, where A is the device area and $I_{light}/(1\ mW/cm^2)$ is the normalized light intensity, is not a constant at

different I_{light}. In terms of the neural network performance, the accuracy obtained with realistic dependence is ~0.9% (~3.1%) lower than that obtained with the ideal linear dependence for recognizing small (large) images (See Figure S16c,d).

18. Data Analysis for Figure S18

The write energy can be calculated from the area enclosed by the loop and the vertical axis (Xu et al., 2017). Based on Figure S18a,b, the write energies are calculated to be ~18 nJ for potentiation and ~23 nJ for depression.

References

Cagin, E., Chen, D.Y., Siddiqui, J.J., and Phillips, J.D. (2007). Hysteretic metal-ferroelectric-semiconductor capacitors based on PZT/ZnO heterostructures. J. Phys. D: Appl. Phys. *40,* 2430.

Choi, S., Tan, S.H., Li, Z., Kim, Y., Choi, C., Chen, P., Yeon, H., Yu, S., and Kim, J. (2018). SiGe Epitaxial Memory for Neuromorphic Computing with Reproducible High Performance Based on Engineered Dislocations. Nat. Mater. *17,* 335–340.

Fridkin, V. M. Bulk photovoltaic effect in noncentrosymmetric crystals. (2001). Crystallogr. Rep. *46,* 654.

Fuller, E.J., Gabaly, F.E., Léonard, F., Agarwal, S., Plimpton, S.J., J.-Gedrim, R.B., James, C.D., Marinella, M.J., and Talin, A.A. (2017). Li-Ion Synaptic Transistor for Low Power Analog Computing. Adv. Mater. *29,* 1604310.

Ge, C., Li, G., Zhou, Q.L., Du, J.Y., Guo, E.J., He, M., Wang, C., Yang, G.Z., and Jin, K.J. (2020). Gating-Induced Reversible H_xVO_2 Phase Transformations for Neuromorphic Computing. Nano Energy *67,* 104268.

Ge, C., Liu, C., Zhou, Q., Zhang, Q., Du, J., Li, J., Wang, C., Gu, L., Yang, G., and Jin, K. (2019). A Ferrite Synaptic Transistor with Topotactic Transformation. Adv. Mater. *31,* 1900379.

Jo, J.Y., Han, H.S., Yoon, J.-G., Song, T.K., Kim, S.-H., and Noh, T.W. (2007). Domain Switching Kinetics in Disordered Ferroelectric Thin Films. Phys. Rev. Lett. *99,* 267602.

Kim, S.S., Kang, T.S., and Je, J.H. (2000). Structures and properties of (001)-oriented $Pb(Zr,Ti)O_3$ films on $LaNiO_3$/Si(001) substrates by pulsed laser deposition. J. Mater. Res. *15,* 2881.

Lee, J., Choi, C.H., Park, B.H., Noh, T.W., and Lee, J.K. (1998). Built-in voltages and asymmetric polarization switching in $Pb(Zr,Ti)O_3$ thin film capacitors. Appl. Phys. Lett. *72,* 3380.

Li, J., Ge, C., Du, J., Wang, C., Yang, G., and Jin, K. (2019). Reproducible Ultrathin Ferroelectric Domain Switching for High-Performance Neuromorphic Computing. Adv. Mater. *32*, 1905764.

Li, T., Sharma, P., Lipatov, A., Lee, H., Lee, J.-W., Zhuravlev, M.Y., Paudel, T.R., Genenko, Y.A., Eom, C.-B., Tsymbal, E.Y., et al. (2017). Polarization-Mediated Modulation of Electronic and Transport Properties of Hybrid MoS_2-$BaTiO_3$-$SrRuO_3$ Tunnel Junctions. Nano Lett. *17*, 922–927.

Ma, C., Luo, Z., Huang, W., Zhao, L., Chen, Q., Lin, Y., Liu, X., Chen, Z., Liu, C., Sun, H., et al. (2020). Sub-Nanosecond Memristor Based on Ferroelectric Tunnel Junction. Nat. Commun. *11*, 1439.

Schatz, A., Pantel, D., and Hanemann, T. (2017). Towards low-temperature deposition of piezoelectric $Pb(Zr,Ti)O_3$: Influence of pressure and temperature on the properties of pulsed laser deposited $Pb(Zr,Ti)O_3$. Thin Solid Films *636*, 680-687.

So, Y.W., Kim, D.J., Noh, T.W., Yoon, J.-G., and Song, T.K. (2005). Polarization Switching Kinetics of Epitaxial $Pb(Zr_{0.4}Ti_{0.6})O_3$ Thin Films. Appl. Phys. Lett. *86*, 092905.

Tagantsev, A.K., Stolichnov, I., Setter, N., and Cross, J.S. (2004). Nature of nonlinear imprint in ferroelectric films and long-term prediction of polarization loss in ferroelectric memories. J. Appl. Phys. *96*, 6616.

Tan, Z., Hong, L., Fan, Z., Tian, J., Zhang, L., Jiang, Y., Hou, Z., Chen, D., Qin, M., Zeng, M., et al. (2019). Thinning Ferroelectric Films for High-Efficiency Photovoltaics Based on the Schottky Barrier Effect. NPG Asia Mater. *11*, 20.

van de Burgt, Y., Lubberman, E., Fuller, E.J., Keene, S.T., Faria, G.C., Agarwal, S., Marinella, M.J., Talin, A.A., and Salleo, A. (2017). A non-volatile organic electrochemical device as a low-voltage artificial synapse for neuromorphic computing. Nat. Mater. *16*, 414-418.

Xu, B., Íñiguez, J., and Bellaiche, L. (2017). Designing lead-free antiferroelectrics for energy storage. Nat. Commun. *8*, 15682.

Yan, F., Sterianou, I., Miao, S., Reaney, I.M., Lai, M.O., and Lu, L. (2010). Multiferroic properties of $Bi(Fe_{0.5}Sc_{0.5})O_3$-$PbTiO_3$ thin films. Phys. Scr. *T139*, 014003.

Yang, C., Shang, D., Liu, N., Fuller, E.J., Agrawal, S., Talin, A.A., Li, Y., Shen, B., and Sun, Y. (2018). All-Solid-State Synaptic Transistor with Ultralow Conductance for Neuromorphic Computing. Adv. Funct. Mater. *28*, 1804170.

Yang, T.-H., Harn, Y.-W., Chiu, K.-C., Fana, C.-L., and Wu, J.-M. (2012). Promising electron field emitters composed of conducting perovskite $LaNiO_3$ shells on ZnO nanorod arrays. J. Mater. Chem. 22, 17071-17078.

Yu, Y.H., Lai, M.O., and Lu, L. (2007). Highly (100) oriented $Pb(Zr_{0.52}Ti_{0.48})O_3/LaNiO_3$ films grown on amorphous substrates by pulsed laser deposition. Appl. Phys. A *88*, 365–370.

Zhou, Y., Chan, H.K., Lam, C.H., and Shin, F.G. (2005). Mechanisms of imprint effect on ferroelectric thin films. J. Appl. Phys. *98*, 024111.